Parity-Reduced Invariant Symmetry Model

Finite Parity-Projection Dynamics, Antipodal Hypercube Quotients, and Formal Verification over $\mathbb{F}_2$

Alexander Sellmeier
Independent Researcher, Munich, Germany

Abstract

Coarse-graining complex systems almost always trades exactness for approximation. Here we show that over binary state spaces, a minimal parity-feedback rule produces exact coarse-graining endogenously, realizing an explicit algebraic connection across discrete dynamical systems, error-correcting codes, spectral graph theory, and quantum information.

Given an n-bit state, the rule flips every bit if the total parity is odd and leaves it unchanged if even. Although simple to state, its behavior splits sharply by coordinate-count parity: it is reversible for even n, yet acts as an idempotent antipodal quotient for odd $n \geq 3$. Under symmetric two-node coupling, just two updates compress exponentially large state spaces (2^{2n} states) onto a single fixed point for even n, or onto an exact four-state parity law for odd n in which the two initial parity bits determine every $2n$-bit state from the second update onward.

Generalizing to arbitrary m-node networks yields an exact rank law for state compression at every time step and proves when node parities alone recover the full network state. In matrix space, the same operator characterizes the $[9, 4, 4]_2$ even-weight product code and maps single-bit matrices bijectively onto four-bit plaquettes.

To ground every layer rigorously, we provide machine-checked Lean 4 proofs for the core algebraic, coupled, product-code, and network recurrence and sufficient-recovery theorems, controlled benchmarks up to $n = 11$ showing a 1.69× matched full-output speedup and a 14,651.7× four-anchor evaluation speedup, and explicit correspondences to quantum channel configurations.

Contents

1 Introduction **4**
- 1.1 The parity-feedback mechanism . . . 4
- 1.2 Core novelties and roadmap . . . 4
- 1.3 Architecture and epistemic scope . . . 5

2 Model and Algebraic Preliminaries **6**

3 Three-Bit Parity Projector **6**
- 3.1 Definition and basic identities . . . 6
- 3.2 Image, kernel, idempotence, and fibres . . . 6
- 3.3 Linear representation . . . 7

4 Affine Single-Node Dynamics **7**

5 Coupled Two-Node Dynamics **8**
- 5.1 Total-parity conservation . . . 8
- 5.2 Exact two-step reduction . . . 8
- 5.3 Sector dynamics for odd shifts . . . 8

6 Exact Four-State Quotient **9**
- 6.1 Parity-pair projection and reduced update . . . 9
- 6.2 Section and exact factorisation . . . 9
- 6.3 Eventual involution, fibre cardinalities, and range compression . . . 10

7 Shift Conjugacy and Classification **10**

8 General-Coordinate Structure, Antipodal Quotients, and Universal Odd-n Reduction **11**
- 8.1 Even/odd coordinate-count dichotomy and minimality of $n = 3$ . . . 11
- 8.2 Antipodal hypercube quotient and canonical direct-sum decomposition . . . 11
- 8.3 Metric and spectral geometry of the folded-cube quotient . . . 13
- 8.4 Universal odd-n coupled reduction and affine two-step retraction . . . 15
- 8.5 Universal even-n two-step constant collapse and partial-agreement criteria . . . 17

9 Multi-Node Graph-Coupled Dynamics and $\mathbb{F}_2$ Rank-Image Laws **18**
- 9.1 Graph-coupled update and split-coordinate decoupling . . . 18
- 9.2 Classification of representative interaction graphs . . . 20

10 Computational Verification and Benchmark Scaling **21**
- 10.1 Domain-boundary audit and workload confounds . . . 21
- 10.2 Matched-workload timing and peak-memory scaling . . . 22

11 Operator-Space Structure **24**
- 11.1 Two-dimensional product-code structure and plaquette duality . . . 24

12 Lean Formalisation and Verification Scope **26**
12.1 Module registry . . . 26
12.2 Claim and theorem registry . . . 27
12.3 Verification scope and submission . . . 28

13 Future Directions **29**
13.1 Further folded-cube geometry and formalization . . . 29
13.2 Observable and dynamic capacity . . . 29
13.3 Directed, weighted, and asynchronous network couplings . . . 30
13.4 Discriminating controls . . . 30

14 Related Work **30**

15 Interfaces and Limitations **32**
15.1 Stabilizer measure-and-feedforward quantum channel bridge . . . 32
15.1.1 Channel 1: Single-node parity-measurement and conditional bit-flip channel $\mathcal{E}_{M_n}$ . . . 32
15.1.2 Channel 2: Coupled two-node coherent syndrome-reset channel $\mathcal{E}^{\text{coherent}}_{T_{n,s}}$ 33
15.1.3 Digital circuit compilation, parity-gate decoder, and resource comparison . . . 35
15.2 Factor-dynamics interface and model limitations . . . 38

16 Conclusion **38**

1 Introduction

1.1 The parity-feedback mechanism

How can a finite microscopic state space collapse onto a tiny closed set of observables without losing algebraic exactness? PRISM (Parity-Reduced Invariant Symmetry Model) addresses this question over the binary field $\mathbb{F}_2$ [1] using a single parity-controlled update. On $V_n := \mathbb{F}_2^n$ with global parity $p_n(x) := x_0 + \cdots + x_{n-1}$ and all-ones vector $\mathbf{1}_n$, the local projector and its symmetric two-node coupling are defined by

$$M_n(x) := x + p_n(x)\mathbf{1}_n, \qquad T_{n,s}(a,b) := \big(M_n(a) + b + s,\, M_n(b) + a + s\big). \tag{1}$$

Because $1 + 1 = 0$ in characteristic two, applying M_n changes every coordinate's parity sum by $(n+1)p_n(x) \pmod 2$. This single arithmetic identity splits the model into two contrasting regimes: for even n, M_n is a self-inverse bijection ($M_n^2 = \mathrm{id}$), whereas for odd $n \geq 3$, M_n becomes an idempotent projector onto the even-parity subspace $\ker(p_n)$ that identifies each state with its bitwise complement. Under two-node coupling $T_{n,s}$, the coarse-grained four-state quotient is not imposed externally; it emerges endogenously from Equation (1) in two microscopic updates.

1.2 Core novelties and roadmap

The manuscript develops five interconnected contributions across §§2–15, deferring full proofs and technical details to the respective sections:

(1) **Odd/even parity dichotomy and folded-cube geometry (Sections 3, 4, 8 and 8.3):** The $n = 3$ projector M is minimal nontrivial within the family M_n, while general odd n yields the direct-sum splitting $V_n = \ker(p_n) \oplus \langle \mathbf{1}_n \rangle$ and canonical representatives of the antipodal hypercube quotient $Q_n/\langle C_n \rangle$, together with its exact quotient Hamming metric and character spectrum $\lambda_j = n - 4j \equiv n \pmod 4$ (checked through $n = 12$).

(2) **Universal four-state collapse, shift conjugacy, and graph nilpotency (Sections 5 to 7, 8.5 and 9):** Two coupled updates collapse all 2^{2n} state pairs to a single constant state for even n, and onto an exact four-state parity quotient $B = \mathbb{F}_2 \times \mathbb{F}_2$ for odd n, with all shift parameters affinely conjugate. On arbitrary m-node graphs with adjacency matrix A, the dynamics decouples into parity propagation under A and internal cancellation under $I + A$, giving an exact step-t image cardinality and proving uniform parity recovery iff $I + A$ is nilpotent over $\mathbb{F}_2$.

(3) **Operator-space product-code and plaquette duality (Sections 11 and 11.1):** Bilateral sandwiching $\mathcal{P}(A) = M_{\mathrm{mat}} A M_{\mathrm{mat}}$ on $\mathrm{Mat}_3(\mathbb{F}_2)$ realizes the $[9, 4, 4]_2$ two-dimensional even-weight product code $\ker(p_3) \otimes \ker(p_3)$, decomposes into $S_3 \times S_3$ and D_4 symmetry orbits, and maps weight-1 basis matrices bijectively onto weight-4 outer-product plaquettes.

(4) **Algorithmic acceleration and quantum-information bridge (Sections 10 and 15):** Controlled benchmarks up to $n = 11$ (4,194,304 state pairs) establish a 1.69× full-materialization speedup and a 14,651.7× speedup (86,580× lower peak memory) when computing the four reachable anchors. On finite-dimensional Hilbert spaces,

two explicit CPTP stabilizer Kraus channels (a single-node parity-measurement channel $\mathcal{E}_{M_n}$ and a two-node coherent reset channel $\mathcal{E}^{\text{coherent}}_{T_{n,s}}$ that protects a two-qubit logical subsystem against node-wise even-weight bit flips) compile into standard digital CNOT circuits as well as an interleaved nearest-neighbor stabilizer chain.

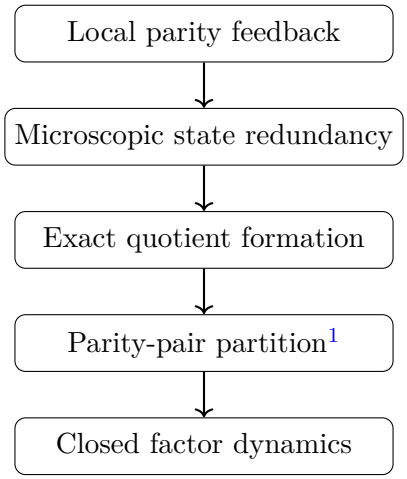
(5) **Machine-checked Lean 4 formalization (Section 12):** Ten Lean 4 modules verify the core $n = 3$ theory, shift conjugacy, linear-map structure and product-code properties, general-dimension dichotomy, universal odd/even coupled theorems, and graph split-coordinate recurrences without `sorryAx` or custom axioms.

1.3 Architecture and epistemic scope

Within this framework, the coarse-grained sectors arise directly from the coupled update through the exact quotient identities

$$\pi \circ T_s = g_{p(s)} \circ \pi, \qquad T_s^2 = \iota_s \circ \pi,$$

structured along five logical stages:



Throughout the manuscript we keep five epistemic roles distinct: model definitions are explicit choices; mathematical consequences are proved from those choices; finite checks and benchmarks are reproducible computations on finite state spaces; Lean 4-verified statements are those covered by the reported build in Section 12; and interfaces or conjectures are never promoted to automatic consequences of the classical $\mathbb{F}_2^n$ model. No claim in the mathematical core derives physical spacetime, quantum measurement, an observer ontology, consciousness, or continuum dynamics; where quantum channels are constructed in Section 15, they are explicit Hilbert-space bridges with stated error-model limits.

[1]The parity-pair partition is respected by the update: T_s maps the fibre over $q \in B$ into the fibre over $g_{p(s)}(q)$. The two total-parity sectors $P(a, b) = p(a) + p(b) \in \mathbb{F}_2$ are forward-invariant.

2 Model and Algebraic Preliminaries

Let

$$V_3 := \mathbb{F}_2^3, \qquad p(x) := x_0 + x_1 + x_2, \qquad \mathbf{1} := (1,1,1),$$

and define the bitwise complement $C(x) := x + \mathbf{1}$. All arithmetic in vector coordinates is over $\mathbb{F}_2$, so $u + u = 0$.

The basic PRISM projector is

$$M : V_3 \to V_3, \qquad M(x) := x + p(x)\mathbf{1}. \tag{2}$$

The choice of V_3, p, and M is a model definition. There are eight states, but the number of coordinates, vector-space dimension, subspace dimension, finite cardinality, operator-space dimension, and iteration index are distinct notions and will not be conflated.

For later comparison, let

$$V_n := \mathbb{F}_2^n, \qquad p_n(x) := \sum_{i=0}^{n-1} x_i, \qquad M_n(x) := x + p_n(x)\mathbf{1}_n, \qquad C_n(x) := x + \mathbf{1}_n.$$

The coupled state space is $W_6 := V_3 \times V_3$, and in general dimension $W_{2n} := V_n \times V_n$. We write coordinatewise binary addition simply as $+$.

3 Three-Bit Parity Projector

3.1 Definition and basic identities

The projector in Equation (2) adds one global parity bit to every coordinate. Its key cancellation is

$$p(M(x)) = 0.$$

Indeed, $p(M(x)) = p(x) + 3p(x) = 4p(x) = 0$ in characteristic two. Hence every output has even parity, while every even-parity input is fixed because $p(x) = 0$ implies $M(x) = x$.

Proposition 3.1 (Idempotence)**.** For every $x \in V_3$, $M(M(x)) = M(x)$.

Proof. The first application produces an even-parity state, and M fixes every even-parity state. □

3.2 Image, kernel, idempotence, and fibres

The image is exactly

$$\mathrm{Im}(M) = \ker p = \{000, 011, 101, 110\}.$$

Exactness is important: even parity is not merely a necessary condition for being an output. It is also sufficient because every even state is fixed by M.

The kernel is

$$\ker M = \{000, 111\}.$$

Moreover, complementation flips parity but leaves the projection unchanged:

$$p(C(x)) = p(x) + 1, \qquad M(C(x)) = M(x).$$

The converse also holds:

$$M(x) = M(y) \quad \Longleftrightarrow \quad y = x \text{ or } y = C(x). \tag{3}$$

Thus every fibre has exactly two distinct elements, a state and its bitwise complement. For $n = 3$, M may therefore be read as choosing the unique even-parity representative of each complement class. In Section 8 we prove that this antipodal hypercube quotient structure extends symbolically to every odd coordinate count n.

3.3 Linear representation

In the standard basis, M is represented by

$$M_{\mathrm{mat}} = I_3 + \mathbf{1}\mathbf{1}^{\mathsf{T}} = \begin{pmatrix} 0 & 1 & 1 \\ 1 & 0 & 1 \\ 1 & 1 & 0 \end{pmatrix}.$$

The current formalization also bundles p and M as linear maps over ZMod(2). The range of the bundled M has cardinality four. This is a finite range-cardinality statement; it should not be confused with a separately formalized finrank theorem.

4 Affine Single-Node Dynamics

For a fixed shift $s \in V_3$, define

$$F_s(x) := M(x) + s. \tag{4}$$

This is another explicit model choice. Its output parity is fixed by the parameter:

$$p(F_s(x)) = p(s).$$

Consequently the image of F_s is exactly the four-state parity coset $\{y : p(y) = p(s)\}$.

A direct calculation gives

$$F_s^2(x) = M(x) + p(s)\mathbf{1},$$

and on the target parity coset this second iterate is the identity. Therefore

$$F_s^3 = F_s. \tag{5}$$

After the first update every orbit is either stationary or has exact period two. More precisely, the displacement of an output under one further step is $M(s)$, so outputs are fixed exactly when $M(s) = 0$. If $M(s) \neq 0$, every reached output belongs to a strict two-cycle. Under the additional hypothesis $p(s) = 1$, the only fixed-output exception is $s = 111$.

The iteration count is not stored in V_3. A two-cycle records only a finite phase. An unbounded event label must be introduced explicitly, as is done by the iteration-index lift discussed in Section 11.

5 Coupled Two-Node Dynamics

On $W_6 = V_3 \times V_3$, define the simultaneous symmetric update

$$T_s(a, b) := (M(a) + b + s,\ M(b) + a + s). \tag{6}$$

This six-coordinate state space has 64 states. Define total parity by

$$P(a, b) := p(a) + p(b).$$

5.1 Total-parity conservation

The node parities evolve by crossing and adding the shift parity:

$$p(T_s(a, b)_1) = p(b) + p(s), \qquad p(T_s(a, b)_2) = p(a) + p(s).$$

Adding these identities cancels the two copies of $p(s)$, yielding

$$P(T_s(a, b)) = P(a, b) \tag{7}$$

for every shift, not only odd shifts. The full space therefore decomposes into two invariant total-parity sectors, each containing 32 states.

5.2 Exact two-step reduction

Define the parity anchor

$$\alpha_s(c) := s + (p(s) + c)\mathbf{1}.$$

It has parity c. The key structural identity is

$$T_s^2(a, b) = (\alpha_s(p(a)), \alpha_s(p(b))). \tag{8}$$

Thus after two steps the system no longer depends on the microscopic representatives within the two initial parity fibres. Only the pair $(p(a), p(b))$ remains relevant. This is an exact algebraic information loss statement, not a sampled observation.

A useful one-step identity explains the mechanism: after one update, the two corresponding coordinates sum to the conserved total parity. At the next update the shared projected component occurs twice and cancels in characteristic two. This cancellation motivates the compression language, while Equation (8) is the theorem that carries the claim.

5.3 Sector dynamics for odd shifts

Assume now $p(s) = 1$. Then $\alpha_s(1) = s$ and $\alpha_s(0) = C(s)$. The two conserved sectors exhibit different attractor structures.

If $P(a, b) = 1$, then $T_s^2(a, b)$ is either $(s, C(s))$ or $(C(s), s)$. Both are fixed points, they are distinct, and there are no other fixed points of T_s. Each step-two preimage class has 16 states.

If $P(a, b) = 0$, then $T_s^2(a, b)$ is either (s, s) or $(C(s), C(s))$. These two synchronized

states form a strict period-two orbit:

$$(s, s) \longmapsto (C(s), C(s)) \longmapsto (s, s).$$

Pairwise complementation commutes with T_s for every shift. Historical Lean declaration names containing `spacetime_mirror_duality` express only identities among update, node swap, and complement operations on these finite attractors; no physical spacetime action is defined by them.

6 Exact Four-State Quotient

6.1 Parity-pair projection and reduced update

Let

$$B := \mathbb{F}_2 \times \mathbb{F}_2, \qquad \pi(a, b) := (p(a), p(b)),$$

where B denotes the four-state parity-pair alphabet (formalized as `ParityPair` in Lean and kept distinct from the hypercube graph notation Q_n in Section 8), and, for $p_s \in \mathbb{F}_2$, define

$$g_{p_s}(q_1, q_2) := (q_2 + p_s, q_1 + p_s).$$

The projection is an exact factor map in the standard sense of semiconjugacy [2, Definition 7.3.3]:

$$\pi(T_s(z)) = g_{p(s)}(\pi(z)). \tag{9}$$

Hence the four-state parity-pair evolution is closed after a single microscopic update.

6.2 Section and exact factorisation

Define the canonical section

$$\iota_s(q_1, q_2) := (\alpha_s(q_1), \alpha_s(q_2)).$$

It satisfies

$$\pi \circ \iota_s = \mathrm{id}_B,$$

so ι_s is injective and π is surjective. More strongly,

$$T_s^2 = \iota_s \circ \pi. \tag{10}$$

This identity makes the two-step collapse completely explicit: the microscopic state is projected to its parity pair and then lifted to a canonical representative.

On the anchor image the microscopic and reduced updates intertwine:

$$T_s(\iota_s(q)) = \iota_s(g_{p(s)}(q)).$$

Since $g_{p(s)}$ is an involution, the four anchor states contain the complete asymptotic dynamics.

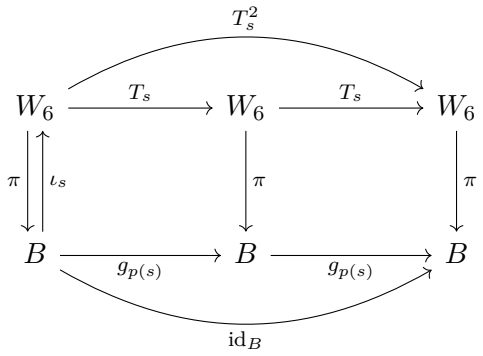


Figure 1: Commutative factor diagram illustrating the exact two-step factorization $T_s^2 = \iota_s \circ \pi$, semiconjugacy $\pi \circ T_s = g_{p(s)} \circ \pi$, and section identity $\pi \circ \iota_s = \mathrm{id}_B$. The 64-state coupled dynamics T_s on W_6 projects via π onto the 4-state reduced dynamics $g_{p(s)}$ on B, while the section ι_s lifts quotient states back to canonical anchors in W_6.

6.3 Eventual involution, fibre cardinalities, and range compression

For every shift and every microscopic state,

$$T_s^4(z) = T_s^2(z). \tag{11}$$

This identity permits both fixed points and two-cycles; it does not assert that every state is stationary after two steps.

The quotient B has four states (`parityPair_card`). Each fibre $\pi^{-1}(q)$ has exactly 16 states (`parityProj_fibre_card`), and

$$T_s^2(z) = \iota_s(q) \iff \pi(z) = q \quad (\texttt{coupledUpdate_two_eq_anchorLift_iff}).$$

For a fixed anchor this fibre is its attraction basin; for an anchor on a two-cycle it is one step-two phase class, while the attraction basin of the periodic orbit is the union of the two associated classes.

Furthermore, exhaustive kernel-checked range counts establish the exact two-step state-space compression across all shifts $s \in V_3$: starting from $|W_6| = 64$ (`coupledState_card`), the one-step image has cardinality $|\operatorname{range}(T_s)| = 16$ (`coupledUpdate_range_card`) and the two-step image has cardinality $|\operatorname{range}(T_s^2)| = 4$ (`coupledUpdate_two_range_card`).

7 Shift Conjugacy and Classification

For $r \in V_3$, define

$$R_r(a, b) := (a + M(r),\, b + r).$$

Because binary addition is self-inverse, $R_r^2 = \mathrm{id}$. For arbitrary shifts s, t, let $r = s + t$. The current formalization proves

$$T_t \circ R_{s+t} = R_{s+t} \circ T_s. \tag{12}$$

Thus all eight shift choices give conjugate finite dynamical systems after a bijective relabeling of the 64 states.

The observable sector labels require a finer statement. Under R_r, first-node parity is

unchanged while second-node parity changes by $p(r)$, and hence

$$P(R_r(z)) = P(z) + p(r).$$

Therefore the supplied conjugacy preserves total-parity sectors exactly when $p(s) = p(t)$. If the shift parities differ, the unlabeled functional graphs remain conjugate but the two parity-sector labels are exchanged. The result is dynamical equivalence under relabeling, not a claim of physical equivalence.

8 General-Coordinate Structure, Antipodal Quotients, and Universal Odd-n Reduction

8.1 Even/odd coordinate-count dichotomy and minimality of $n = 3$

For $V_n = \mathbb{F}_2^n$, define $M_n(x) = x + p_n(x)\mathbf{1}_n$. Its output parity obeys

$$p_n(M_n(x)) = (n+1)\, p_n(x) \quad (\texttt{parityN_M_N}),$$

with the integer coefficient interpreted in $\mathbb{F}_2$. This yields the fundamental even/odd coordinate-count dichotomy.

Proposition 8.1 (Even coordinate count)**.** If n is even, then $M_n^2 = \mathrm{id}_{V_n}$. Consequently, M_n is a self-inverse bijection with trivial kernel.

Lean support: `M_N_even_involution`, `M_N_even_bijective`, `M_N_even_kernel_trivial`.

Proposition 8.2 (Odd coordinate count and minimality of $n = 3$ within M_n)**.** If n is odd, then $p_n(M_n(x)) = 0$, $M_n^2 = M_n$, and $M_n(\mathbf{1}_n) = \mathbf{0}_n$. Moreover:

1. For $n = 1$, M_1 collapses every state to zero.
2. For $n = 2$, M_2 is an involution rather than a non-injective projection.
3. For $n = 3$, M_3 is a non-trivial idempotent projector.

Thus, within the parity-projector family M_n, $n = 3$ is the minimal positive coordinate count for which M_n acts as a non-trivial idempotent parity projector. In the Lean development, `minimal_nontrivial_projective_dimension` packages the zero case $n = 1$, involutivity at $n = 2$, and the non-trivial idempotent case $n = 3$ (together with annihilation of $\mathbf{1}_3$) as a conjunction of case facts supporting this minimality argument within the family M_n, rather than as an unconstrained existential minimum across all projective operators.

Lean support: parity identity: `parityN_M_N_odd`; idempotence: `M_N_odd_idempotent`; constant-one image: `M_N_odd_constant_one`; $n = 1$: `M_1_trivial`; $n = 2$: `M_N_even_involution`; $n = 3$: `M_3_nontrivial`.

8.2 Antipodal hypercube quotient and canonical direct-sum decomposition

Equip $V_n = \mathbb{F}_2^n$ with the structure of the n-dimensional binary hypercube Q_n, where two states are adjacent when they differ in exactly one coordinate. The bitwise complement involution

$$C_n(x) := x + \mathbf{1}_n$$

maps each vertex $x \in Q_n$ to its unique antipodal vertex at Hamming distance n. Denote the two-element antipodal equivalence class of x by

$$[x] := x + \langle \mathbf{1}_n \rangle = \{x,\, x + \mathbf{1}_n\} \in V_n/\langle \mathbf{1}_n \rangle.$$

Here $V_n/\langle \mathbf{1}_n \rangle$ denotes the vector-space quotient by the repetition subspace. The folded-cube graph $Q_n/\langle C_n \rangle$ has the same vertex classes, with adjacency inherited from hypercube edges; this graph structure is distinct from the quotient vector-space structure.

Theorem 8.3 (Antipodal quotient realization and direct-sum splitting)**.** Let $n \geq 1$ be odd. Then:

(1) $p_n(C_n(x)) = p_n(x) + 1$ and $M_n(C_n(x)) = M_n(x)$.

(2) The image of M_n is exactly the even-parity hyperplane

$$\mathrm{Im}(M_n) = \ker(p_n),$$

its kernel is the repetition subspace

$$\ker(M_n) = \{\mathbf{0}_n, \mathbf{1}_n\} = \langle \mathbf{1}_n \rangle,$$

and the fibres of M_n are precisely the antipodal classes:

$$M_n(x) = M_n(y) \quad \Longleftrightarrow \quad y = x \ \text{ or } \ y = C_n(x). \tag{13}$$

(3) Consequently, M_n induces a canonical bijection

$$\overline{M}_n : V_n/\langle \mathbf{1}_n \rangle \xrightarrow{\sim} \ker(p_n), \qquad [x] \longmapsto M_n(x),$$

and V_n decomposes into the internal direct sum

$$V_n = \ker(p_n) \oplus \langle \mathbf{1}_n \rangle \cong (V_n/\langle \mathbf{1}_n \rangle) \times \mathbb{F}_2, \qquad x = M_n(x) + p_n(x)\mathbf{1}_n, \tag{14}$$

via the coordinate map

$$x \longmapsto \big(M_n(x), p_n(x)\big).$$

Its injectivity is formalized as `direct_sum_injective_N`, and surjectivity is formalized as `direct_sum_surjective_N`, since every pair $(u, c) \in \ker(p_n) \times \mathbb{F}_2$ is represented by

$$x = u + c\mathbf{1}_n.$$

Proof. Since n is odd, $p_n(\mathbf{1}_n) = n \equiv 1 \pmod 2$. Linearity gives $p_n(x + \mathbf{1}_n) = p_n(x) + 1$, whence $M_n(x + \mathbf{1}_n) = x + \mathbf{1}_n + (p_n(x) + 1)\mathbf{1}_n = x + p_n(x)\mathbf{1}_n = M_n(x)$. If $p_n(y) = 0$, then $M_n(y) = y$, so $\mathrm{Im}(M_n) = \ker(p_n)$. If $M_n(x) = M_n(y)$, then $y = x + (p_n(x) + p_n(y))\mathbf{1}_n$, which equals x when $p_n(x) = p_n(y)$ and $C_n(x)$ when $p_n(x) \neq p_n(y)$. Thus M_n factors through $V_n/\langle \mathbf{1}_n \rangle$ as a bijection onto $\ker(p_n)$, and $x = M_n(x) + p_n(x)\mathbf{1}_n$ gives the direct-sum decomposition since $\ker(p_n) \cap \langle \mathbf{1}_n \rangle = \{\mathbf{0}_n\}$. □

Lean support: (1) parity: `parityN_complementN_odd`; (1) complement invariance: `M_N_odd_complementN`; (2) image: `M_N_odd_image_iff_even`; (2) kernel: `M_N_odd_kernel_iff`; (2) fibres: `M_N_odd_same_image_iff`.

Corollary 8.4 (Canonical even-parity representative)**.** For odd n, every antipodal hypercube class $[x] = \{x, x + \mathbf{1}_n\}$ contains a unique even-parity state, and that state is $M_n(x)$.

Lean support: `canonical_even_representative_odd`.

Geometrically, identifying antipodal vertices $x \sim x+\mathbf{1}_n$ folds the hypercube Q_n onto the simple folded-cube graph $\square_n := Q_n/\langle C_n\rangle$ [3]. Within Q_n itself, $\ker(p_n)$ has no Hamming-distance-one edges; the graph adjacency on the even-parity representatives in $\ker(p_n)$ is obtained by transporting the simple quotient-graph adjacency of $\square_n$ via $\overline{M}_n$, with Cayley generators $M_n(e_i) = e_i + \mathbf{1}_n$ for odd $n \geq 3$. While the graph quotient $Q_n/\langle C_n\rangle$ is defined for every $n \geq 1$ (Table 1), Theorem 8.3 shows that the parity projector M_n realizes the antipodal vertex quotient if and only if n is odd; for even n, $\mathbf{1}_n \in \ker(p_n)$ and M_n is a bijection of the vertex set V_n.

n	Antipodal quotient $Q_n/\langle C_n\rangle$	Action of parity operator M_n
1	K_1 (single vertex)	Zero projector onto $\ker(p_1) = \{0\}$
2	K_2	Vertex-set involution ($M_2^2 = \mathrm{id}$, not a quotient map)
3	K_4 (complete graph on 4 vertices)	Canonical projector onto $\ker(p_3)$ (transported K_4 adjacency; core PRISM)
4	$K_{4,4}$ (complete bipartite graph)	Vertex-set involution ($M_4^2 = \mathrm{id}$, not a quotient map)
5	Folded 5-cube SRG$(16, 5, 0, 2)$	Canonical projector onto $\ker(p_5)$
6	Folded 6-cube (32 vertices)	Vertex-set involution ($M_6^2 = \mathrm{id}$, not a quotient map)
7	Folded 7-cube (64 vertices)	Canonical projector onto $\ker(p_7)$
8	Folded 8-cube (128 vertices)	Vertex-set involution ($M_8^2 = \mathrm{id}$, not a quotient map)

Table 1: Antipodal hypercube quotients $Q_n/\langle C_n\rangle$ and their realization by M_n at odd n.

8.3 Metric and spectral geometry of the folded-cube quotient

The antipodal quotient carries a metric inherited from the prescribed Hamming coordinates [3]. This metric exists for every $n \geq 1$, while its realization on even-parity representatives by M_n retains the odd-n hypothesis of Theorem 8.3.

Theorem 8.5 (Quotient Hamming metric and character spectrum)**.** On $V_n/\langle \mathbf{1}_n\rangle$ for $n \geq 1$, the formula

$$d_Q([x], [y]) = \min\{\mathrm{wt}(x + y),\ n - \mathrm{wt}(x + y)\} \tag{15}$$

defines a metric equal to shortest-path distance in the simple folded-cube graph, with diameter $\lfloor n/2\rfloor$. The graph has 2^{n-1} vertices, degree 0 at $n = 1$, degree 1 at $n = 2$, and degree n for $n \geq 3$. For $n \geq 3$, its adjacency spectrum consists of

$$\lambda_j = n - 4j, \qquad \text{multiplicity } \binom{n}{2j}, \qquad 0 \leq 2j \leq n. \tag{16}$$

In particular, every eigenvalue is congruent to n modulo 4.

Proof. Complementing either representative exchanges the two entries of the minimum, so the distance is well-defined. Its zero classes are precisely antipodal pairs. For the triangle inequality, choose complement offsets attaining the distances from $[x]$ to $[y]$ and from $[y]$ to $[z]$. Their sum is an allowed complement offset from x to z; the Hamming triangle

inequality bounds that candidate and hence also the minimum. A shortest Hamming path to a minimizing representative projects to a quotient path of this length. Conversely, every quotient path lifts to coordinate flips ending at one of the two representatives, so it cannot be shorter. The diameter and degrees follow, with loops and duplicate edges removed at $n = 1, 2$.

The characters of V_n descending to the quotient are exactly $\chi_a([x]) = (-1)^{a \cdot x}$ with $p_n(a) = 0$. They give all 2^{n-1} characters of the quotient. For $n \geq 3$, the coordinate-flip classes are distinct nonzero generators, so the adjacency eigenvalue is $\sum_i (-1)^{a_i} = n - 2\,\mathrm{wt}(a)$. Even character weight $\mathrm{wt}(a) = 2j$ gives Equation (16), with the stated binomial multiplicities. □

Table 2 records the finite dimension range checked independently by breadth-first search and character sums in `notebooks/experiments/PRISM/tier-c-extensions/`. All binary differences and quotient edges were included at $n = 1, \ldots, 12$; Cayley translation reduces arbitrary vertex pairs to these differences. The metric and spectral statements are analytical results, not additional Lean declarations. At $n = 3$ the quotient is K_4, at $n = 4$ it is $K_{4,4}$, and at $n = 5$ its strongly regular parameters are $(16, 5, 0, 2)$. Naming conventions differ: Brouwer calls its 10-regular complement the Clebsch graph and notes that other authors use that name for the folded five-cube [4]. We use the parameters to specify the graph.

n	1	2	3	4	5	6	7	8	9	10	11	12
Vertices	1	2	4	8	16	32	64	128	256	512	1024	2048
Degree	0	1	3	4	5	6	7	8	9	10	11	12
Diameter	0	1	1	2	2	3	3	4	4	5	5	6

Table 2: Simple antipodal-quotient graph parameters checked across $n = 1, \ldots, 12$.

Remark 8.6 (Modular spectrum and code orthogonality). The spectral congruence in Equation (16) implies $4 \mid \lambda_j$ at $n = 4, 8, 12$, but it does not imply self-orthogonality of the full even-weight code $H_n = \ker(p_n)$ under the binary dot product. For every $n \geq 3$, $110 \cdots 0$ and $101 \cdots 0$ belong to H_n and have dot product 1. The parity-operator columns $g_i = M_n(e_i) = e_i + \mathbf{1}_n$ have Gram entries $g_i \cdot g_i = n - 1 \pmod 2$ and $g_i \cdot g_j = n - 2 \pmod 2$ for $i \neq j$; at positive even n this Gram matrix is the identity. The valid coding distinction is that the repetition code $R_n = \langle \mathbf{1}_n \rangle$ is self-orthogonal exactly when n is even, and doubly even (all weights divisible by four) exactly when $4 \mid n$ [5]. This leaves room for separately specified self-orthogonal subcodes. These metric and coding statements preserve coordinate permutations, not arbitrary linear changes that fail to preserve the declared Hamming metric or dot product.

Example 8.7 (A selected Hamming/Fano subcode at $n = 7$)**.** Choose an external 3×7 parity-check matrix P with all nonzero columns of $\mathbb{F}_2^3$, and set $C = \ker(P)$, the $[7, 4, 3]_2$ Hamming code [5]. Its 16 words have enumerated weight polynomial $W_C(z) = 1 + 7z^3 + 7z^4 + z^7$, while the 8 words of its simplex dual have $W_{C^\perp}(z) = 1 + 7z^4$. The seven weight-three supports form the Fano lines. The rows of P have weight four and pairwise intersection two, so $C^\perp \subset C \cap \ker(p_7)$. Both spaces have dimension three: P has rank three, and $\mathbf{1}_7 \in C$ has odd parity. Thus

$$M_7(C) = C^\perp, \qquad C/\langle \mathbf{1}_7 \rangle \cong C^\perp,$$

realizing a self-orthogonal $[7,3,4]_2$ subcode even though the full $[7,6,2]_2$ even-weight space is not self-orthogonal. The code C is dual-containing, not self-dual. The parity-check matrix is additional structure: M_7 alone selects neither this Hamming code nor its Fano incidence system. The example is a scoped coding-theoretic connection, checked by complete finite enumeration, rather than an intrinsic geometric selection or a new-code claim.

8.4 Universal odd-n coupled reduction and affine two-step retraction

On the 2^{2n}-state coupled space $W_{2n} = V_n \times V_n$, define the simultaneous symmetric update

$$T_{n,s}(a,b) := \big(M_n(a) + b + s,\ M_n(b) + a + s\big), \tag{17}$$

total parity $P_n(a,b) := p_n(a) + p_n(b)$, factor projection $\pi_n(a,b) := (p_n(a), p_n(b)) \in B = \mathbb{F}_2 \times \mathbb{F}_2$, parity anchor $\alpha_{n,s}(c) := s + (p_n(s) + c)\mathbf{1}_n$, and canonical lift $\iota_{n,s}(q_1,q_2) := (\alpha_{n,s}(q_1), \alpha_{n,s}(q_2))$.

Theorem 8.8 (Universal odd-n two-step factorization)**.** For every odd coordinate count $n \geq 1$ and every shift $s \in V_n$:

(1) Total parity is conserved: $P_n(T_{n,s}(a,b)) = P_n(a,b)$, with no restriction on $p_n(s)$, since the two shift contributions sum to $2p_n(s) = 0$ in $\mathbb{F}_2$.

(2) The parity-pair map $\pi_n : W_{2n} \to B$ commutes in one step with $T_{n,s}$ and the reduced involution $g_{p_n(s)}(q_1,q_2) = (q_2 + p_n(s), q_1 + p_n(s))$:

$$\pi_n \circ T_{n,s} = g_{p_n(s)} \circ \pi_n, \qquad \pi_n \circ \iota_{n,s} = \mathrm{id}_B\,.$$

(3) Two coupled updates factor exactly through the four-state quotient B and satisfy eventual involution:

$$T_{n,s}^2 = \iota_{n,s} \circ \pi_n, \qquad T_{n,s}^4 = T_{n,s}^2. \tag{18}$$

Proof. Using $b = M_n(b) + p_n(b)\mathbf{1}_n$ and $a = M_n(a) + p_n(a)\mathbf{1}_n$ from Equation (14), the first update takes the form

$$T_{n,s}(a,b) = \big([M_n(a) + M_n(b)] + p_n(b)\mathbf{1}_n + s,\ [M_n(a) + M_n(b)] + p_n(a)\mathbf{1}_n + s\big). \tag{19}$$

Applying p_n to each component and using $p_n(M_n(\cdot)) = 0$ and $p_n(\mathbf{1}_n) = 1$ gives $\pi_n(T_{n,s}(a,b)) = (p_n(b) + p_n(s),\ p_n(a) + p_n(s)) = g_{p_n(s)}(\pi_n(a,b))$. Moreover, the sum of the two components of $T_{n,s}(a,b)$ is $(p_n(a) + p_n(b))\mathbf{1}_n = P_n(a,b)\mathbf{1}_n$ because the shared folded-cube term $M_n(a) + M_n(b)$ and shift s cancel in characteristic two. At the second update, applying M_n to the first component annihilates $(p_n(b)\mathbf{1}_n)$ and adds it to the second component, canceling $M_n(a) + M_n(b)$ completely and leaving $(\alpha_{n,s}(p_n(a)),\ \alpha_{n,s}(p_n(b))) = \iota_{n,s}(\pi_n(a,b))$. □

Lean support: (1) total parity: `totalParityN_preserved_odd`; (2) semiconjugacy: `parityProjN_coupledUpdateN_odd`; (2) section: `parityProjN_anchorLiftN_odd`; (3) two-step factorization: `coupledUpdateN_two_eq_anchorLiftN_parityProjN`; (3) eventual involution: `coupledUpdateN_four_eq_two_odd`.

Theorems 8.3 and 8.8 clarify the exact relationship between the two distinct reductions present in PRISM:

- **Symmetry reduction ($2^n \to 2^{n-1}$ per node; $2^{2n} \to 2^{2n-2}$ on W_{2n}):** Induced by the node-wise parity projector $\mu_n(a,b) = (M_n(a), M_n(b))$, which retains the $2(n-1)$ bits of even-parity coordinates in $\ker(p_n) \times \ker(p_n)$ and erases the 2-bit parity pair $\pi_n(a,b) \in B$.

- **Dynamical reduction ($2^{2n} \to 2^{n+1} \to 4$ on W_{2n}):** Induced by the coupled evolution $T_{n,s}$. Let $H := \ker(p_n)$ (of size $h = 2^{n-1}$) and write states in split coordinates via Equation (14) as $a = u + c\mathbf{1}_n$, $b = v + d\mathbf{1}_n$, and $s = w + e\mathbf{1}_n$, where the internal coordinates $u = M_n(a)$, $v = M_n(b)$, and $w = M_n(s)$ lie in H, and the parity bits $c = p_n(a)$, $d = p_n(b)$, and $e = p_n(s)$ lie in $\mathbb{F}_2$. By Equation (19) and Theorem 8.8, the first and second iterates take the normal form

$$\begin{aligned} T_{n,s}(u,v;c,d) &= (u+v+w,\ u+v+w;\ d+e,\ c+e), \\ T_{n,s}^2(u,v;c,d) &= (w,w;\ c,d). \end{aligned} \tag{20}$$

  (formalized as `nodeProjectorN_coupledUpdateN_odd` and `coupledUpdateN_two_split_coords_odd`). After one step, the common even-parity component $u+v+w$ ranges over all of H (for example by varying $u \in H$ at $v = 0$) independently of the output parity pair $(d+e, c+e) = g_e(c,d)$, which ranges over all of $B = \mathbb{F}_2^2$ since g_e is bijective. Because split coordinates uniquely distinguish states in W_{2n}, the one-step image has exact cardinality $4 \cdot 2^{n-1} = 2^{n+1}$ (giving $64 \to 16 \to 4$ at $n = 3$ and $4 \to 4 \to 4$ at $n = 1$). At step two, $u + v$ cancels and the image is the four-state affine plane $A_s := \mathrm{Im}(\iota_{n,s}) = \{(w,w)\} \times B$ (`mem_anchor_set_iff_odd`).

- **First-entry time into the anchor set A_s:** By Equation (20), a state $z = (u,v;c,d)$ already belongs to A_s at step 0 if and only if $u = v = w$ (4 states). Its one-step image $T_{n,s}(z)$ belongs to A_s if and only if $u+v+w = w$, that is, $u = v$ (`coupledUpdateN_mem_anchor_set_iff_odd`). Consequently, the first entry time into A_s is 0 if $u = v = w$ (4 states), 1 if $u = v$ and $u \neq w$ ($4(h-1)$ states), and 2 if $u \neq v$ ($4h(h-1)$ states). For odd $n \geq 3$, $h \geq 4$ so the uniform bound of two steps is sharp; for $n = 1$, $H = \{0\}$ and every state starts in A_s. Reaching the individual anchor $\iota_{n,s}(\pi_n(z))$ at step two reflects the intermediate swap of the parity coordinates at step one.

Thus the dynamical factor map π_n does not factor through the diagonal antipodal quotient map $\alpha_{\mathrm{diag}}(a,b) = \{(a,b),(C_n(a),C_n(b))\}$ because $C_n \times C_n$ flips both node parities: $\pi_n(C_n(a),C_n(b)) = \pi_n(a,b) + (1,1) \neq \pi_n(a,b)$. Instead, π_n is $\mathbb{Z}_2$-equivariant under diagonal complementation. In split coordinates on $W_{2n} \cong H^2 \oplus B$, the node-wise projection is the linear map $\mu_n(u,v;c,d) = (u,v;0,0)$, whereas the two-step map $T_{n,s}^2(u,v;c,d) = (w,w;c,d)$ is an affine retraction onto A_s (which is linear at the origin if and only if $w = M_n(s) = \mathbf{0}_n$, i.e. $s \in \{\mathbf{0}_n, \mathbf{1}_n\}$). Defining the self-inverse centering translation $\Lambda_s(u,v;c,d) := (u+w, v+w; c, d)$, which commutes with μ_n, conjugates this affine retraction to the complementary linear projection:

$$(\Lambda_s \circ T_{n,s}^2 \circ \Lambda_s)(u,v;c,d) = (0,0;c,d) \quad (\texttt{shiftCenterTransN_conjugates_two_step_odd}).$$

8.5 Universal even-n two-step constant collapse and partial-agreement criteria

For positive even coordinate counts n, the single-node operator M_n is a self-inverse bijection ($M_n^2 = \mathrm{id}_{V_n}$) because $\mathbf{1}_n \in \ker(p_n)$ satisfies $p_n(\mathbf{1}_n) = n \equiv 0 \pmod 2$. Under the symmetric two-node coupling $T_{n,s}$, however, this parity conservation of M_n produces a stronger two-step collapse than in the odd-n case: instead of retaining the four-state parity quotient B, the two-step map collapses the entire 2^{2n}-state space onto a single constant state.

Theorem 8.9 (Universal even-n two-step constant collapse and partial-agreement fractions)**.** Let $n \geq 2$ be even and let $s \in V_n$. Write $c = p_n(a)$, $d = p_n(b)$, $e = p_n(s)$, and $z = a + b + s$. Then for all $(a, b) \in W_{2n}$:

(1) **One-step parity synchronization and zero total parity:** Because $p_n(M_n(x)) = p_n(x)$ for even n, the first update $T_{n,s}(a, b) = (z + c\,\mathbf{1}_n,\ z + d\,\mathbf{1}_n)$ assigns identical parities to both nodes and annihilates total parity in one step:

$$p_n(T_{n,s}(a,b)_1) = p_n(T_{n,s}(a,b)_2) = c + d + e, \qquad P_n(T_{n,s}(a,b)) = 0. \tag{21}$$

(2) **Two-step constant collapse:** At the second update, $T_{n,s}^2$ is the constant map

$$T_{n,s}^2(a,b) = (s + e\,\mathbf{1}_n,\ s + e\,\mathbf{1}_n) = (M_n(s),\ M_n(s)), \qquad |\mathrm{Im}(T_{n,s}^2)| = 1, \tag{22}$$

which is a fixed point of $T_{n,s}$ ($T_{n,s}(M_n(s), M_n(s)) = (M_n(s), M_n(s))$).

(3) **Exact partial-agreement criteria on W_{2n}:**

(a) Two-step total-parity preservation holds if and only if the initial node parities agree:

$$P_n(T_{n,s}^2(a,b)) = P_n(a,b) \quad \Longleftrightarrow \quad p_n(a) = p_n(b),$$

which is satisfied by exactly half (2^{2n-1} out of 2^{2n}, or 50%) of initial state pairs.

(b) The odd-n one-step parity rule $g_e(\pi_n(a,b)) = (d + e,\ c + e)$ agrees with the actual one-step parity pair $\pi_n(T_{n,s}(a,b)) = (c + d + e,\ c + d + e)$ if and only if both initial nodes have even parity:

$$\pi_n(T_{n,s}(a,b)) = g_{p_n(s)}(\pi_n(a,b)) \quad \Longleftrightarrow \quad p_n(a) = 0 \ \text{ and } \ p_n(b) = 0,$$

which is satisfied by exactly one quarter (2^{2n-2} out of 2^{2n}, or 25%) of initial state pairs.

(c) The odd-n two-step anchor formula $\iota_{n,s}(\pi_n(a,b)) = (\alpha_{n,s}(c), \alpha_{n,s}(d))$ agrees with $T_{n,s}^2(a,b) = (M_n(s), M_n(s))$ if and only if $c = d = 0$ (25% of pairs); by contrast, the naive parity-after-two-steps identity $\pi_n(T_{n,s}^2(a,b)) = \pi_n(a,b)$ reduces to $(e,e) = (c,d)$, which holds if and only if $c = d = e$ (25% of pairs).

Proof. Since n is even, $p_n(\mathbf{1}_n) = 0$ and $p_n(M_n(x)) = p_n(x) + p_n(x)p_n(\mathbf{1}_n) = p_n(x)$. Expanding $T_{n,s}(a,b)_1 = a + c\,\mathbf{1}_n + b + s = z + c\,\mathbf{1}_n$ and $T_{n,s}(a,b)_2 = z + d\,\mathbf{1}_n$ gives Equation (21) immediately upon applying p_n. Substituting $a' = z + c\,\mathbf{1}_n$ and $b' = z + d\,\mathbf{1}_n$ with common parity $p_n(a') = p_n(b') = c + d + e$ into the second update yields

$$T_{n,s}^2(a,b)_1 = (z + c\,\mathbf{1}_n) + (c + d + e)\mathbf{1}_n + (z + d\,\mathbf{1}_n) + s = s + e\,\mathbf{1}_n = M_n(s)$$

because $z+z=\mathbf{0}_n$ and $(c+c+d+d)\mathbf{1}_n=\mathbf{0}_n$ over $\mathbb{F}_2$, and identically $T^2_{n,s}(a,b)_2=M_n(s)$. Since $P_n(M_n(s),M_n(s))=e+e=0$, $P_n(T^2_{n,s}(a,b))=P_n(a,b) \iff c+d=0 \iff c=d$. Similarly, $(c+d+e,\ c+d+e)=(d+e,\ c+e) \iff c=0$ and $d=0$. Since $p_n: V_n\to\mathbb{F}_2$ is a non-zero linear functional for $n\geq 2$, $|\ker(p_n)|=2^{n-1}$, so $c=d$ holds on $2\cdot(2^{n-1})^2=2^{2n-1}$ pairs (50%) and $c=d=0$ holds on $(2^{n-1})^2=2^{2n-2}$ pairs (25%). □

Lean support: even-n parity invariance: `parityN_M_N_even`; (1) one-step parities and total parity: `coupledUpdateN_parity_fst_even`, `coupledUpdateN_parity_snd_even`, `totalParityN_coupledUpdateN_even`; (2) two-step constant collapse: `coupledUpdateN_two_even`; (3a) total-parity agreement criterion: `totalParityN_two_eq_initial_iff_even`; (3b) one-step odd-rule agreement criterion: `parityProjN_coupledUpdateN_eq_odd_rule_iff_even`.

9 Multi-Node Graph-Coupled Dynamics and $\mathbb{F}_2$ Rank-Image Laws

The two-node coupled system $T_{n,s}$ on $W_{2n}=V_n\times V_n$ corresponds to the single-edge complete graph $G=K_2$ with binary adjacency matrix $A_{K_2}=\left(\begin{smallmatrix}0&1\\1&0\end{smallmatrix}\right)$. We now generalize this coupling to an arbitrary m-node simple undirected graph $G=(V,E)$ and establish a complete algebraic classification of its image-cardinality trajectory and exact parity-quotient recovery for odd n [6, 7, 3].

9.1 Graph-coupled update and split-coordinate decoupling

Definition 9.1 (Graph-coupled PRISM dynamics)**.** Let $G=(V,E)$ be a simple undirected graph on $m=|V|$ vertices $\{0,1,\dots,m-1\}$ with binary adjacency matrix $A\in\mathbb{F}_2^{m\times m}$ ($A_{uv}=1$ if $\{u,v\}\in E$ and 0 otherwise, with $A_{vv}=0$). On the m-node configuration space $V_n^m=(\mathbb{F}_2^n)^m$ with shift vector $s=(s_0,\dots,s_{m-1})\in V_n^m$, define the synchronous update $T_{G,s}: V_n^m\to V_n^m$ at each vertex $v\in V$ by

$$T_{G,s}(x)_v := M_n(x_v)+\sum_{u\in V} A_{vu}\,x_u+s_v. \tag{23}$$

Let $\pi_{G,n}: V_n^m\to\mathbb{F}_2^m$ denote the node-wise parity projection $\pi_{G,n}(x):=(p_n(x_0),\dots,p_n(x_{m-1}))^{\mathsf{T}}$.

Theorem 9.2 (Split-coordinate decoupling, $\mathbb{F}_2$ rank-image law, and nilpotent recovery criterion)**.** Let $n\geq 1$ be odd, and let $G=(V,E)$ be an m-node simple undirected graph with adjacency matrix $A\in\mathbb{F}_2^{m\times m}$ and shift $s\in V_n^m$. Decompose each vertex state via Equation (14) as $x_v=y_v+q_v\mathbf{1}_n$ and shift as $s_v=w_v+e_v\mathbf{1}_n$, where $y_v=M_n(x_v), w_v=M_n(s_v)\in H:=\ker(p_n)$ and $q_v=p_n(x_v), e_v=p_n(s_v)\in\mathbb{F}_2$. Then:

(1) **Universal graph semiconjugacy and channel decoupling:** Under $T_{G,s}$, the parity vector $q^{(t)}=\pi_{G,n}(T^t_{G,s}(x))\in\mathbb{F}_2^m$ and the internal even-parity vector $y^{(t)}=(M_n(T^t_{G,s}(x)_v))_{v\in V}\in H^m$ evolve autonomously and without cross-talk according to the affine matrix recurrences over $\mathbb{F}_2$:

$$q^{(t+1)}=A\,q^{(t)}+e,\qquad y^{(t+1)}=(I+A)\,y^{(t)}+w. \tag{24}$$

In particular, $\pi_{G,n}\circ T_{G,s}=g_{G,e}\circ\pi_{G,n}$ with $g_{G,e}(q):=Aq+e$ holds for every graph G.

(2) **Exact step-t image cardinality formula:** Because $\dim_{\mathbb{F}_2}(H) = n-1$ and the shift translation preserves affine subspace dimension, the exact number of reachable full states after $t \geq 0$ updates is

$$\left|\mathrm{Im}(T^t_{G,s})\right| = 2^{\,\mathrm{rank}_{\mathbb{F}_2}(A^t) \,+\, (n-1)\,\mathrm{rank}_{\mathbb{F}_2}((I+A)^t)}. \tag{25}$$

(3) **Complete nilpotency criterion for uniform parity recovery ($n \geq 3$):** For odd $n \geq 3$ (whereas at $n = 1$, $H = \{0\}$ and $\pi_{G,1}(x)$ already specifies the full state on every graph), the t-step full state $T^t_{G,s}(x)$ is uniquely determined by the initial parity vector $q^{(0)} = \pi_{G,n}(x)$ (independently of the initial $m(n-1)$ internal bits $y^{(0)} \in H^m$) if and only if

$$(I + A)^t = 0 \pmod 2. \tag{26}$$

Thus the full network state eventually becomes recoverable from $\pi_{G,n}(x)$ alone if and only if $I+A$ is nilpotent over $\mathbb{F}_2$, and its nilpotency index $k = \min\{t \geq 1 : (I+A)^t = 0\}$ is the earliest uniform recovery time. Whenever $(I + A)^k = 0 \pmod 2$:

(a) $A = I + (I + A)$ is invertible over $\mathbb{F}_2$ (with inverse $A^{-1} = \sum_{j=0}^{k-1}(I + A)^j$), so $\mathrm{rank}_{\mathbb{F}_2}(A^t) = m$ for all $t \geq 0$ and all 2^m parity vectors survive: $\left|\mathrm{Im}(T^k_{G,s})\right| = 2^m$.

(b) The k-step map factors exactly as $T^k_{G,s} = \iota^{(k)}_{G,s} \circ \pi_{G,n}$, where the canonical k-step anchor lift $\iota^{(k)}_{G,s} : \mathbb{F}_2^m \hookrightarrow V_n^m$ is given explicitly by

$$\iota^{(k)}_{G,s}(q) = \sum_{j=0}^{k-1}(I + A)^j M_n(s) \;+\; \Big(A^k q + \sum_{j=0}^{k-1} A^j p_n(s)\Big)\mathbf{1}_n. \tag{27}$$

(c) In particular, uniform two-step collapse ($k = 2$) occurs if and only if $(I + A)^2 = I + A^2 = 0 \pmod 2$, i.e., $A^2 = I \pmod 2$.

Proof. Substituting $x_u = y_u + q_u\mathbf{1}_n$ and $s_v = w_v + e_v\mathbf{1}_n$ into Equation (23) and using $M_n(x_v) = y_v$ gives

$$T_{G,s}(x)_v = \Big(y_v + \sum_{u\in V} A_{vu}y_u + w_v\Big) + \Big(\sum_{u\in V} A_{vu}q_u + e_v\Big)\mathbf{1}_n.$$

Since $H = \ker(p_n)$ is a linear subspace of V_n, the first parenthesized sum lies in H. For odd n, $p_n(h) = 0$ for all $h \in H$, $p_n(\mathbf{1}_n) = 1$, and $M_n(\mathbf{1}_n) = \mathbf{0}_n$. Applying p_n and M_n node-wise therefore extracts $q^{(t+1)} = Aq^{(t)} + e$ and $y^{(t+1)} = (I + A)y^{(t)} + w$, proving (1). Iterating Equation (24) t times yields the affine expressions

$$q^{(t)} = A^t q^{(0)} + \sum_{j=0}^{t-1} A^j e, \qquad y^{(t)} = (I + A)^t y^{(0)} + \sum_{j=0}^{t-1}(I + A)^j w.$$

Because the direct-sum map $V_n^m \cong \mathbb{F}_2^m \oplus H^m$ is a linear isomorphism and $H \cong \mathbb{F}_2^{n-1}$ causes $(I + A)^t$ to act diagonally across $n-1$ independent binary coordinates, the linear part of $T^t_{G,s}$ has image dimension $\mathrm{rank}_{\mathbb{F}_2}(A^t) + (n-1)\,\mathrm{rank}_{\mathbb{F}_2}((I + A)^t)$, which establishes Equation (25). Finally, since $n \geq 3$ implies $\dim_{\mathbb{F}_2}(H) = n - 1 \geq 2 > 0$, $y^{(t)}$ is independent of $y^{(0)} \in H^m$ if and only if $(I + A)^t = 0$ over $\mathbb{F}_2$. In characteristic two, $(I + A)^k = 0$ implies

$A\sum_{j=0}^{k-1}(I+A)^j = (I+(I+A))\sum_{j=0}^{k-1}(I+A)^j = I+(I+A)^k = I$, so A is invertible and Equation (27) follows immediately. □

9.2 Classification of representative interaction graphs

Theorem 9.2 explains how graph topology controls the balance between parity propagation (A^t) and internal even-parity cancellation ($(I+A)^t$). Table 3 and Figure 2 report the exact trajectories verified exhaustively across six representative graphs at $n = 3$ (up to $2^{12} = 4{,}096$ states) together with even-$n = 4$ controls in `notebooks/experiments/PRISM/graph-coupled-dynamics/`:

- **Two-step involutive graphs ($A^2 = I \implies (I+A)^2 = 0$, index $k = 2$):** On both $G = K_2$ ($m = 2$) and the 4-clique $G = K_4$ ($m = 4$), every vertex has odd degree and every pair of distinct vertices shares an even number of common neighbors, so $A^2 = I \pmod 2$. The internal register $(I+A)^2 y^{(0)} = 0$ vanishes in two steps: K_2 compresses $64 \to 16 \to 4 = 2^2$ states, while K_4 compresses $4{,}096 \to 64 \to 16 = 2^4$ states.
- **Higher-index Jordan-nilpotent collapse ($(I+A)^4 = 0$, index $k = 4$):** On the 4-node `Paw` graph (a triangle $\{0,1,2\}$ with a pendant leaf 3 attached to vertex 2), $(I+A)^2 \neq 0$ and $(I+A)^3 \neq 0$: the two-step image retains 256 states ($\operatorname{rank}(A^2) = 4$, $\operatorname{rank}((I+A)^2) = 2$, giving $2^{4+2\cdot 2} = 256$) and the three-step image retains 64 states ($\operatorname{rank}((I+A)^3) = 1$, giving $2^{4+2\cdot 1} = 64$). Because $I+A$ has nilpotency index $k = 4$ over $\mathbb{F}_2$, the internal coordinates decay stepwise ($\operatorname{rank}((I+A)^t) = 4,3,2,1,0$ for $t = 0,1,2,3,4$), yielding exact 16-state parity recovery at step $t = 4$:

$$4{,}096 \longrightarrow 1{,}024 \longrightarrow 256 \longrightarrow 64 \longrightarrow 16 = 2^4.$$

- **Partial rank plateaus ($0 < \operatorname{rank}((I+A)^t) < m$):** On the 4-star $K_{1,3}$ and triangle K_3, neither A nor $I+A$ is nilpotent; the dynamics stabilizes at $t = 2$ (64 states on $K_{1,3}$) and $t = 1$ (16 states on K_3), retaining both partial parity and partial internal degrees of freedom.
- **Dual parity collapse ($A^2 = 0 \implies (I+A)^2 = I$):** On the 4-cycle C_4, every pair of vertices has an even number of common neighbors and every vertex has even degree 2, so $A^2 = 0 \pmod 2$ while $(I+A)^2 = I$. This reverses the PRISM mechanism: after two steps the parity register is completely erased ($\operatorname{rank}(A^2) = 0$, fixing $q^{(2)} = Ae + e$), while all $4(n-1) = 8$ bits of internal even-parity structure evolve bijectively ($4{,}096 \to 1{,}024 \to 256 = 2^8$ states).
- **Even-n control ($n = 4$):** For even n, $p_n(\mathbf{1}_n) = 0$ couples the internal difference into the parity update while M_n acts as $I + \mathbf{1}_n\mathbf{1}_n^{\mathsf{T}}$; at $n = 4$, K_2 collapses to 1 state at $t = 2$ ($256 \to 16 \to 1$) by Theorem 8.9, K_4 collapses to 1 state at $t = 2$ ($65{,}536 \to 64 \to 1$), and K_3 stabilizes at 16 states ($4{,}096 \to 64 \to 16$).

Graph G	m	n	$\operatorname{rank}_{\mathbb{F}_2}(A^t)$ $(t = 0..4)$	$\operatorname{rank}_{\mathbb{F}_2}((I+A)^t)$ $(t = 0..4)$	Image trajectory $\lvert\operatorname{Im}(T^t_{G,s})\rvert$	Uniform parity recovery
K_2	2	3	$2,2,2,2,2$	$2,1,0,0,0$	$64 \to 16 \to 4 \to 4 \to 4$	**Yes** ($k = 2$, $2^2 = 4$)
K_4	4	3	$4,4,4,4,4$	$4,1,0,0,0$	$4096 \to 64 \to 16 \to 16 \to 16$	**Yes** ($k = 2$, $2^4 = 16$)
`Paw`	4	3	$4,4,4,4,4$	$4,3,2,1,0$	$4096 \to 1024 \to 256 \to 64 \to 16$	**Yes** ($k = 4$, $2^4 = 16$)
$K_{1,3}$	4	3	$4,2,2,2,2$	$4,3,2,2,2$	$4096 \to 256 \to 64 \to 64 \to 64$	No (plateau at 64)
K_3	3	3	$3,2,2,2,2$	$3,1,1,1,1$	$512 \to 16 \to 16 \to 16 \to 16$	No (plateau at 16)
C_4	4	3	$4,2,0,0,0$	$4,4,4,4,4$	$4096 \to 1024 \to 256 \to 256 \to 256$	Dual ($A^2 = 0$, $2^8 = 256$)
K_2^*	2	4^*	$2,2,2,2,2$	$2,1,0,0,0$	$256 \to 16 \to 1 \to 1 \to 1$	Constant (1 state at $t = 2$)

Table 3: Multi-node graph-coupled trajectories $|\mathrm{Im}(T^t_{G,s})|$ for $t = 0, \ldots, 4$ and $\mathbb{F}_2$ matrix-power ranks from Theorem 9.2 (*even-$n = 4$ control).

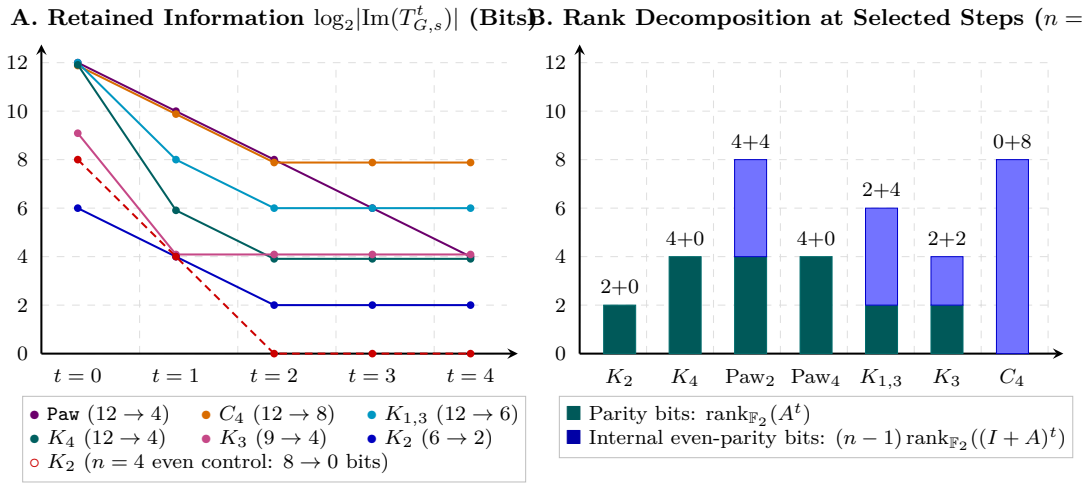


Figure 2: Multi-node graph-coupled PRISM dynamics (Theorem 9.2). **(A)** Retained information $\log_2|\mathrm{Im}(T^t_{G,s})|$ across steps $t = 0, \ldots, 4$ for six graphs at $n = 3$ and the even-$n = 4$ control on K_2. **(B)** Rank decomposition at selected steps into retained parity bits $\mathrm{rank}_{\mathbb{F}_2}(A^t)$ and internal even-parity bits $(n-1)\,\mathrm{rank}_{\mathbb{F}_2}((I+A)^t)$ (labeled above each bar as parity + internal), contrasting two-step collapse on K_4, four-step Jordan-nilpotent collapse on `Paw`, and dual parity erasure ($A^2 = 0$) on C_4.

10 Computational Verification and Benchmark Scaling

While the theorems in Sections 3 to 8 establish exact symbolic identities over $\mathbb{F}_2$, finite computational experiments serve two complementary purposes: (i) empirically auditing domain boundaries and counterexamples when hypotheses (such as odd n) are violated, and (ii) quantifying the algorithmic time and memory savings achieved by the quotient factorization $T^2_{n,s} = \iota_{n,s} \circ \pi_n$ under controlled workload definitions.

10.1 Domain-boundary audit and workload confounds (`PRISM/parity-quotient`)

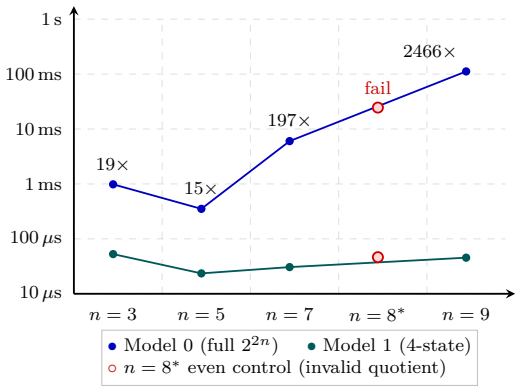
In the first computational study (`notebooks/experiments/PRISM/parity-quotient/`), the full 2^{2n}-state microscopic evolution (`Model 0`) was compared against the 4-state quotient reduction (`Model 1`) across odd dimensions $n \in \{3, 5, 7, 9\}$ and the even negative-control dimension $n = 8$ (65,536 state pairs) at shift $s = (0, \ldots, 0, 1)$. As shown in Figure 3, every odd dimension passes all four universal identities across 100% of state pairs, whereas $n = 8$ fails as a universal identity with the explicit minimal counterexample $a = 00000000$, $b = 00000001$, $s = 00000001$, where

$$T^2_{8,s}(a, b) = (11111110,\, 11111110) \;\neq\; (11111110,\, 00000001) = \iota_{8,s}(\pi_8(a, b)).$$

Crucially, the reduced 4-state map $g_c(q_1, q_2) = (q_2 + c, q_1 + c)$ remains a valid self-inverse involution ($g_c^2 = \mathrm{id}_B$) at $n = 8$ because its definition on $\mathbb{F}_2^2$ does not depend on n; what fails at even n is the homomorphism $\pi_n \circ T_{n,s} = g_{p_n(s)} \circ \pi_n$ linking the quotient to the

microscopic system. In exact agreement with Theorem 8.9(3), exhaustive enumeration at $n = 8$ confirms that two-step total-parity preservation holds on 32,768/65,536 pairs (50%, where $p_8(a) = p_8(b)$) and the odd-n one-step parity rule holds on 16,384/65,536 pairs (25%, where $p_8(a) = p_8(b) = 0$).

A. Recorded Single-Run Workload Time



B. Verification Matrix & Even-n Fractions

Check	$n = 3$	$n = 5$	$n = 7$	$n = 9$	$n = 8^*$
Total parity P_n	100%	100%	100%	100%	50%
Quotient $g_c^2 = \mathrm{id}$	PASS	PASS	PASS	PASS	PASS
Step-1 rule $g_c \circ \pi_n$	100%	100%	100%	100%	25%
Step-2 rule $\iota_{n,s} \circ \pi_n$	100%	100%	100%	100%	25%
$\lvert\mathrm{Im}(T^2_{n,s})\rvert$	4	4	4	4	1

Even $n = 8^*$: $T^2_{8,s}(a,b) = (M_8(s), M_8(s))$ collapses all 65,536 pairs to 1 constant state; P_8 holds iff $p_8(a) = p_8(b)$ (50%), step-1 and step-2 odd rules iff $p_8(a) = p_8(b) = 0$ (25%).

Figure 3: Domain-boundary and single-run workload audit (`PRISM/parity-quotient`). **(A)** Single-run elapsed time across $n \in \{3, 5, 7, 8^*, 9\}$, illustrating the $n = 3 > n = 5$ cold-start anomaly eliminated in the multi-trial benchmark of Figure 4. **(B)** Universal pass rates and exact even-$n = 8$ partial-agreement fractions (Theorem 8.9).

Panel A of Figure 3 also exposes an instructive benchmarking lesson: in a single-run unpacked script that includes state-grid allocation inside the timer, $n = 3$ (982 μs) appears slower than $n = 5$ (414 μs) due to first-call NumPy allocator and page-fault cold-start overhead, and comparing a full 2^{2n}-element table allocation directly against a 4-anchor evaluation conflates two different computational tasks.

10.2 Matched-workload timing and peak-memory scaling (`PRISM/matched-workload-benchmark`)

To isolate the algorithmic effect of the quotient theorem from representation and allocation confounds, the second study (`notebooks/experiments/PRISM/matched-workload-benchmark/`) separates state-grid pre-allocation from timed execution, performs 3 warmup runs followed by 7 timed trials per model with `tracemalloc` peak-memory tracking across $n \in \{3, 5, 7, 8, 9, 11\}$ (up to $2^{22} = 4{,}194{,}304$ state pairs at $n = 11$), and evaluates four distinct implementations across two precisely defined tasks:

- **Task B — Full 2^{2n}-output materialization** (computing the two-step output for every input pair $(a, b) \in W_{2n}$):

  (1) `Model 0a` (*Unpacked array baseline*): $(2^{2n}, n)$ `uint8` coordinate arrays with $O(n \cdot 2^{2n})$ work ($n \leq 9$).

  (2) `Model 0b` (*Bit-packed integer-XOR baseline*): n-bit states packed into `uint32` words using SWAR popcount parity and bitwise XOR in $O(2^{2n})$ word operations.

  (3) `Model 1b` (*Quotient + full 2^{2n} materialization*): Computes the 4 canonical anchors $\iota_{n,s}(q)$ once and indexes them by the initial parity pair $(p_n(a), p_n(b))$ across all 2^{2n} pairs.

- **Task A — Reachable anchor-set computation** (computing the exact image $\mathrm{Im}(T_{n,s}^2) = A_s$ and the 4-state parity lookup table):

  (4) `Model 1a` (*Quotient 4-anchor reduction*): Evaluates $g_{p_n(s)}^2 = \mathrm{id}_B$ and lifts only the 4 parity pairs via $\iota_{n,s}$. The number of anchor states evaluated is $\Theta(1)$ (4 states for every odd n), while representing four explicit $2n$-bit anchor vectors requires $\Theta(n)$ bits ($\Theta(1)$ machine words for $n \leq 32$).

		Median 2-step runtime (7 trials)				Speedup vs. `0b`		Peak update RAM	
n	Pairs 2^{2n}	`Model 0a`	`Model 0b`	`Model 1b`	`Model 1a`	`1b` (full)	`1a` (4-anc.)	`Model 0b`	`Model 1a`
3	64	46.6 μs	47.5 μs	47.1 μs	21.0 μs	1.01×	2.26×	3,344 B	1,744 B
5	1,024	232.7 μs	80.7 μs	64.0 μs	21.2 μs	1.26×	3.81×	37.9 KB	1,744 B
7	16,384	5.09 ms	463.4 μs	274.3 μs	21.4 μs	1.69×	21.65×	590.9 KB	1,744 B
8*	65,536	24.67 ms	2.17 ms	1.42 ms	20.9 μs	(1.53×)	N/A*	2.36 MB	1,744 B
9	262,144	118.08 ms	18.58 ms	9.18 ms	20.5 μs	2.02×	906.3×	9.44 MB	1,744 B
11	4,194,304	—	307.69 ms	181.99 ms	21.0 μs	**1.69**×	**14,651.7**×	**151.0** MB	**1,744** B

Table 4: Matched-workload 2-step update runtime and `tracemalloc` peak memory across $n \in \{3, 5, 7, 8^*, 9, 11\}$ (`PRISM/matched-workload-benchmark`). At even $n = 8^*$, `Model 1a/1b` do not match `Model 0b` (25% agreement; Theorem 8.9).

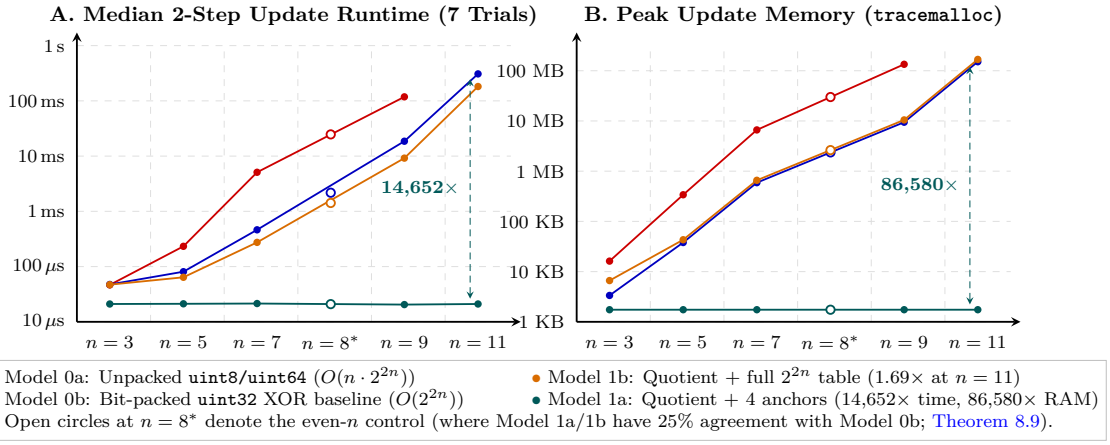


Figure 4: Controlled timing and peak-memory scaling across $n \in \{3, 5, 7, 8^*, 9, 11\}$ (`PRISM/matched-workload-benchmark`, Table 4). **(A)** 7-trial median 2-step runtime on a logarithmic scale, contrasting the 1.69× full-materialization speedup (`Model 1b` vs. `Model 0b`) with the 14,651.7× 4-anchor reduction speedup (`Model 1a` vs. `Model 0b`) at $n = 11$. **(B)** Peak update memory allocation (`tracemalloc`), showing $O(2^{2n})$ scaling for `Model 0b/1b` (151.0 MB and 167.8 MB at $n = 11$) versus constant 1,744 B (86,580× reduction) for `Model 1a`.

Table 4 and Figure 4 establish two distinct, non-competing performance conclusions at $n = 11$ (4,194,304 pairs):

(1) **When every input's output must be materialized in memory (`Model 1b` vs. `Model 0b`):** Replacing two full coupled updates by one parity-table lookup yields a **1.69**× speedup (181.99 ms vs. 307.69 ms; 2.02× at $n = 9$), while using slightly more peak memory (167.8 MB vs. 151.0 MB) due to the intermediate index array $2p_n(a) + p_n(b)$. Both methods remain $\Theta(2^{2n})$ in time and space because writing 2^{2n} outputs dominates the runtime.

(2) **When the reachable attractor set or on-demand parity lookup suffices (`Model 1a` vs. `Model 0b`):** Because Theorem 8.8 guarantees that only 4 anchor states exist at $t = 2$, `Model 1a` runs in **21.0** μs with **1,744** B of peak memory at $n = 11$, delivering a **14,651.7**× runtime speedup and **86,580**× memory reduction over the bit-packed baseline `Model 0b`. In addition, exhaustive all-shift verification confirmed 100% agreement between `Model 0b` and `Model 1b` across all 8 shifts at $n = 3$ (512 pairs) and all 32 shifts at $n = 5$ (32,768 pairs).

11 Operator-Space Structure

The current code bundles four linear maps over ZMod(2): the parity functional p, the projector M, a sandwich operator on binary 3×3 matrices, and a total-entry parity contraction τ. With M_{mat} as defined in Section 3.3, the sandwich map is

$$\mathcal{P}(A) := M_{\text{mat}} A M_{\text{mat}}.$$

It is idempotent (`sandwich_idempotent`). For $A \in \text{Mat}_3(\mathbb{F}_2)$, the scalar contraction is defined explicitly as the total-entry parity contraction

$$\tau(A) := p(A\mathbf{1}) = \mathbf{1}^{\mathsf{T}} A \mathbf{1} = \sum_{i=0}^{2} \sum_{j=0}^{2} A_{ij} \in \mathbb{F}_2.$$

Thus $\tau(A)$ is the sum of all nine matrix entries in $\mathbb{F}_2$ (formalized as the bundled linear map `PRISM.tau_linear`), which is distinct from the ordinary diagonal matrix trace $\text{tr}(A) = \sum_{i=0}^{2} A_{ii}$. Exhaustive finite checks give

$$|\,\text{range}(M)| = 4, \qquad |\,\text{range}(\mathcal{P})| = 16, \qquad |\,\text{range}(\tau)| = 2$$

(`M_linear_range_card`, `sandwich_linear_range_card`, and `tau_linear_range_card`). These are cardinalities of finite ranges. No claim of a formalized module `finrank` is inferred from the counts alone.

Two auxiliary constructions are kept distinct from this operator-space projection. First, the homogeneous state space $V_4 := V_3 \times \mathbb{F}_2$ has 16 states and carries

$$L_s(x, c) := (M(x) + cs, c),$$

where the preserved bit c selects the affine branch $c = 1$ or the pure projector branch $c = 0$. Second, the iteration-index lift $\mathbb{N} \times W_6$ sends (n, z) to $(n + 1, T_s(z))$. The added natural number labels update events; it is not generated from the finite state and does not recover distinctions erased by the dynamics. The full binary 3×3 matrix space has 512 elements.

11.1 Two-dimensional product-code structure and plaquette duality

Because $M_{\text{mat}} = M_{\text{mat}}^{\mathsf{T}}$ projects V_3 onto the $[3, 2, 2]_2$ even-weight code $\ker(p_3)$ along $\langle \mathbf{1}_3 \rangle$, the bilateral sandwich map $\mathcal{P}(A) = M_{\text{mat}} A M_{\text{mat}}$ admits a basis-independent coding-theoretic and geometric characterization.

Theorem 11.1 (Product-code characterization, orbit structure, and plaquette bijection)**.** Let $\mathcal{P}(A) := M_{\text{mat}} A M_{\text{mat}}$ on $\text{Mat}_3(\mathbb{F}_2)$, and more generally let $\mathcal{P}_n(A) := M_n A M_n$ on

$\mathrm{Mat}_n(\mathbb{F}_2)$ for odd $n \geq 3$ ($M_n = I_n + \mathbf{1}_n\mathbf{1}_n^\mathsf{T}$). Then:

(1) **Two-dimensional even-weight product code:** The 16-element image of $\mathcal{P}$ is precisely the $[9, 4, 4]_2$ binary even-weight product code [5]:

$$\mathrm{Im}(\mathcal{P}) = \{B \in \mathrm{Mat}_3(\mathbb{F}_2) \mid B\mathbf{1}_3 = \mathbf{0}_3 \text{ and } \mathbf{1}_3^\mathsf{T} B = \mathbf{0}_3^\mathsf{T}\} = \ker(p_3) \otimes \ker(p_3).$$

Under independent row and column permutations ($S_3 \times S_3$), $\mathrm{Im}(\mathcal{P})$ decomposes into $1 + 9 + 6 = 16$ matrices: the rank-0 weight-0 zero matrix, 9 rank-1 weight-4 four-cycles, and 6 rank-2 weight-6 permutation complements $\mathbf{1}_3\mathbf{1}_3^\mathsf{T} + P_\sigma$ ($\sigma \in S_3$). Under rigid dihedral square symmetries (D_4), these refine into six orbits of sizes $1 + 1 + 2 + 4 + 4 + 4 = 16$.

(2) **Weight-1 site to weight-4 plaquette bijection:** On the nine standard basis matrices $E_{i,j} = e_i e_j^\mathsf{T}$ ($i, j \in \{0, 1, 2\}$),

$$\mathcal{P}(E_{i,j}) = (e_i + \mathbf{1}_3)(e_j + \mathbf{1}_3)^\mathsf{T}$$

maps $E_{i,j}$ bijectively onto the nine rank-1, weight-4 outer-product plaquettes of $\ker(p_3) \otimes \ker(p_3)$. Under D_4, the fixed center matrix $E_{1,1}$ maps to the unique D_4-invariant four-corner frame, the four corner matrices $\{E_{0,0}, E_{0,2}, E_{2,0}, E_{2,2}\}$ map bijectively onto the four contiguous 2×2 blocks, and the four edge-midpoint matrices map onto the four wrap-around 2×2 plaquettes.

(3) **Universal odd-n identity-to-projector trace:** For every odd $n \geq 3$, M_n is symmetric and idempotent, so the identity matrix executes the one-step forward trace

$$I_n \xrightarrow{\mathcal{P}_n} M_n^2 = M_n \xrightarrow{\mathcal{P}_n} M_n, \qquad I_n + M_n = \mathbf{1}_n\mathbf{1}_n^\mathsf{T}.$$

In particular, at $n = 3$, $I_3 \mapsto M_{\mathrm{mat}}$ is a transient entry rather than a fixed point, whereas M_{mat} is an absorbing fixed point ($\mathcal{P}(M_{\mathrm{mat}}) = M_{\mathrm{mat}}$).

Proof. For (1), since M_3 is symmetric and projects onto $\ker(p_3)$ with $\ker(M_3) = \langle \mathbf{1}_3 \rangle$, every $B = M_{\mathrm{mat}} A M_{\mathrm{mat}}$ satisfies $B\mathbf{1}_3 = \mathbf{0}_3$ and $\mathbf{1}_3^\mathsf{T} B = \mathbf{0}_3^\mathsf{T}$. Conversely, any B whose rows and columns all have even parity is fixed by left and right multiplication by M_{mat}, so $\mathrm{Im}(\mathcal{P}) = \ker(p_3) \otimes \ker(p_3)$, which has dimension $(3 - 1)^2 = 4$ and minimum Hamming weight $2 \cdot 2 = 4$. The unique weight-0 element is 0. Each rank-1 matrix in $\ker(p_3) \otimes \ker(p_3)$ has the form uv^T for nonzero $u, v \in \ker(p_3)$ (3 choices each, yielding 9 matrices of weight $2 \cdot 2 = 4$). The remaining $16 - 1 - 9 = 6$ matrices are invertible on $\ker(p_3)$ and arise by complementing the six 3×3 permutation matrices P_σ over $\mathbb{F}_2$ ($\mathbf{1}_3\mathbf{1}_3^\mathsf{T} + P_\sigma$ has row and column sums $3 + 1 \equiv 0 \pmod 2$ and weight 6). Under D_4, the zero matrix and center plaquette form the two size-1 orbits; $\{\mathbf{1}_3\mathbf{1}_3^\mathsf{T} + I_3, \mathbf{1}_3\mathbf{1}_3^\mathsf{T} + J_{\mathrm{anti}}\}$ forms the size-2 rank-2 orbit (since 90° rotation swaps main and anti-diagonal); and the four contiguous 2×2 blocks, four wrap-around plaquettes, and remaining four permutation complements form three size-4 orbits.

For (2), $M_{\mathrm{mat}} e_i = e_i + \mathbf{1}_3$, so $\mathcal{P}(e_i e_j^\mathsf{T}) = (M_{\mathrm{mat}} e_i)(M_{\mathrm{mat}} e_j)^\mathsf{T} = (e_i + \mathbf{1}_3)(e_j + \mathbf{1}_3)^\mathsf{T}$. Because $e_i \mapsto e_i + \mathbf{1}_3$ is a bijection from $\{e_0, e_1, e_2\}$ onto the three nonzero vectors of $\ker(p_3)$, $(i, j) \mapsto \mathcal{P}(E_{i,j})$ is a bijection onto the 9 rank-1 plaquettes, compatible with D_4 since index 1 is the unique midpoint fixed by D_4. For (3), $M_n^\mathsf{T} = M_n$ and odd $n \geq 3$ gives $M_n^2 = M_n$ (Theorem 8.3), whence $\mathcal{P}_n(I_n) = M_n I_n M_n = M_n$, $\mathcal{P}_n(M_n) = M_n^3 = M_n$, and $I_n + M_n = \mathbf{1}_n\mathbf{1}_n^\mathsf{T}$. □

12 Lean Formalisation and Verification Scope

12.1 Module registry

The formalization comprises ten PRISM implementation modules, including the general odd-n antipodal quotient, universal coupled reduction, and graph-coordinate recurrence and recovery extensions. Table 5 records the module index used in the claim registry below together with the verification status.

Table 5: PRISM module registry for the Lean 4 formalization.

No.	Module	Status	Scope / remarks
M1	`PRISM.ParityProjector`	PASS	Three-coordinate parity projector, image, kernel, and fibres.
M2	`PRISM.AffineDynamics`	PASS	Affine single-node dynamics and eventual involution.
M3	`PRISM.CoupledDynamics`	PASS	Coupled update, conserved total parity, two-step anchors, and sector dynamics.
M4	`PRISM.IterationLift`	PASS	Iteration-index lift, homogeneous-coordinate extension, and matrix representation.
M5	`PRISM.FourStateReduction`	PASS	Exact four-state quotient, section, factorisation, fibre cardinalities, and stepwise range counts.
M6	`PRISM.ShiftConjugacy`	PASS	Explicit conjugacy between shift-parametrized coupled systems.
M7	`PRISM.LinearStructure`	PASS	Bundled linear maps, sandwich idempotence, finite range cardinalities, even-row/column image, weights, plaquette identities and injectivity, and odd-n operator-composition traces.
M8	`PRISM.GeneralDimension`	PASS	Even/odd coordinate-count dichotomy, trivial $n = 1$ case, and $n = 3$ minimality.
M9	`PRISM.AntipodalQuotient`	PASS	Symbolic odd-n antipodal fibres, direct-sum decomposition, universal odd-n $T^2_{n,s} = \iota_{n,s} \circ \pi_n$ affine retraction, translation conjugacy, entry-time criteria, and universal even-n two-step constant collapse with partial-agreement criteria.
M10	`PRISM.GraphDynamics`	PASS	Odd-n graph parity/internal recurrences, internal difference propagation, parity determinacy and sufficient nilpotent recovery; K_2, K_4, paw and C_4 matrix identities.

The PRISM entry module importing this set passed compilation using Lean 4 [8] and `mathlib` [9]. The status column refers to the Lean verification of this source revision; which is stated separately in Section 12.3.

12.2 Claim and theorem registry

Table 6 links the principal manuscript claims to the modules in Table 5 and to representative Lean declarations. The registry is intentionally selective: it identifies the formal support for the central mathematical statements without turning the manuscript into an inventory of source-level theorem names.

Table 6: Principal manuscript claims and representative formal support.

Claim	Principal content	Module	Representative Lean declaration(s)
Projector	Idempotence; exact even-parity image; kernel and complementary fibres	M1	`M_idempotent`, `image_iff_even`, `kernel_iff`, `same_image_iff`
Affine dynamics	$F_s^3 = F_s$ and the fixed-output / exact-two-cycle criterion	M2	`affineUpdate_three_eq_one`, `affineUpdate_output_fixed_iff`
Coupled dynamics	Total-parity conservation, exact two-step anchors, and parity-sector dynamics	M3	`totalParity_preserved`, `coupledUpdate_two`, together with the fixed-point and oscillation theorems
Exact quotient	$\pi \circ T_s = g_{p(s)} \circ \pi$, $T_s^2 = \iota_s \circ \pi$, $T_s^4 = T_s^2$, and $64 \to 16 \to 4$ range counts	M5	`parityProj_coupledUpdate`, `coupledUpdate_two_eq_anchorLift_parityProj`, `coupledUpdate_four_eq_two`, `coupledUpdate_range_card`, `coupledUpdate_two_range_card`
Shift conjugacy	Explicit conjugacy of all shift-parametrized coupled systems	M6	`shiftEquiv_conjugates`, `all_shifts_conjugate`
General coordinate count	Even-coordinate involution and trivial kernel; odd-coordinate idempotence; $n = 1$ triviality and $n = 3$ minimality	M8	`M_N_even_involution`, `M_N_even_bijective`, `M_N_even_kernel_trivial`, `M_N_odd_idempotent`, `M_1_trivial`, `M_3_nontrivial`, `minimal_nontrivial_projective_dimension`
Antipodal quotient & odd-n collapse	Odd-n antipodal fibres, direct-sum splitting, universal two-step factorisation $T_{n,s}^2 = \iota_{n,s} \circ \pi_n$, affine retraction, and entry times	M9	`M_N_odd_image_iff_even`, `M_N_odd_same_image_iff`, `direct_sum_injective_N`, `coupledUpdateN_two_eq_anchorLiftN_parityProjN`, `coupledUpdateN_four_eq_two_odd`, `direct_sum_surjective_N`, `coupledUpdateN_two_split_coords_odd`, `shiftCenterTransN_conjugates_two_step_odd`, `coupledUpdateN_mem_anchor_set_iff_odd`

Continued on next page

Table 6 (continued)

Claim	Principal content	Module	Representative Lean declaration(s)
Even-n constant collapse	Universal two-step collapse $T^2_{n,s}(a,b) = (M_n(s), M_n(s))$ and exact 50% / 25% partial-agreement criteria	M9	`parityN_M_N_even`, `coupledUpdateN_parity_fst_even`, `coupledUpdateN_parity_snd_even`, `totalParityN_coupledUpdateN_even`, `coupledUpdateN_two_even`, `totalParityN_two_eq_initial_iff_even`, `parityProjN_coupledUpdateN_eq_odd_rule_iff_even`
Operator layer & product code	Linear maps and cardinalities; even-row/column image, weight bounds, plaquette identities/injectivity, and odd-n traces	M7	`sandwich_image_iff_product_code`, `sandwich_basisMatrix3_injective`, `opSandwichN_id_odd`, and the linear-map, weight and cardinality theorems
Graph coordinates & recovery	Parity evolves under A, internal differences under $(I+A)^t$; $(I+A)^k = 0$ suffices for step-k determination by initial parities at fixed shift	M10	`graphParityProjN_update_odd`, `graphInternalProjN_iter_diff_odd`, `graphCoupledIterN_eq_of_nilpotent_odd`, and the parity-determinacy and benchmark matrix theorems

12.3 Verification scope and submission

The reported verification run has status PASS, exit code zero, and no recorded failures. It used Lean v4.35.0, and the project build completed successfully before fresh checks of the ten implementation modules and the entry module `PRISM.lean` listed in Tables 5–6. A kernel axiom audit (`#print axioms` in `PRISM.lean`) confirmed that all 60 audited principal declarations depend exclusively on Lean's standard foundational axioms (`propext`, `Quot.sound`, and `Classical.choice`), with zero `sorryAx` or custom axioms.

For Theorem 11.1, the formalization now includes the even-row/column image characterization, weight spectrum and minimum nonzero weight, indexed plaquette formula and injectivity, the $n = 3$ matrix trace identities, and the two operator-composition trace identities for every odd n (including $n = 1$). The finite 3×3 statements use kernel-evaluated decision proofs; image membership is derived from idempotence, and the arbitrary odd-n traces are symbolic consequences of `M_N_odd_idempotent`. The abstract tensor-product identification, orbit decompositions, and general matrix identity $I_n + M_n = \mathbf{1}_n \mathbf{1}_n^{\mathsf{T}}$ remain analytical statements rather than additional Lean declarations. The general odd-n image counts and generic-projector comparison follow algebraically from the formalized factorization and one-step formulas.

For the graph dynamics in Theorem 9.2, Lean verifies the one-step parity and internal-coordinate recurrences, propagation of internal differences by $(I+A)^t$, and preservation of equality of initial parity vectors. It also verifies the sufficient recovery statement: at fixed shift, $(I+A)^k = 0$ implies that equal initial node parities give identical step-k states. These symbolic results hold for any binary adjacency matrix, any node count, and every odd coordinate count, including $n = 1$; symmetry and zero diagonal are not required by these declarations. Finite kernel decision proofs check $(I+A)^2 = 0$ for K_2 and K_4, exact

nilpotency index four for the paw, and $A^2 = 0$, $(I + A)^2 = I$ for C_4. The graph rank/image formula, the converse recovery criterion for odd $n \geq 3$, and an explicit reconstruction map remain analytical results. The quantum channel/circuit results in Section 15 remain proved analytically and checked on their specified finite cases. Section 10 reports measured runtimes and peak allocations. No later edits to the Lean sources are asserted here to inherit this status automatically without re-running the audit script.

The verification claim is theorem-specific. A successful Lean build does not establish that the chosen model is unique, physically correct, empirically adequate, or ontologically privileged. Conversely, the absence of a formal theorem for a stronger prose inference does not undermine the verified statements actually present in source.

The manuscript submission package includes the complete Lean sources underlying the reported formalization, together with the Lean toolchain specification, Lake project files and dependency manifest, and the corresponding build and verification records. These ancillary artifacts provide the material needed to inspect and reproduce the reported formal verification under the recorded environment.

13 Future Directions

This section records proposed extensions beyond the completed PRISM theorems.

13.1 Further folded-cube geometry and formalization

The quotient metric, diameter, and character spectrum are established analytically in Theorem 8.5, with finite checks through $n = 12$. Remaining work includes their Lean 4 formalization, classification of face orbits and graph automorphisms, and determining which geometric structures the PRISM update itself selects. These questions should be compared directly with standard folded-cube graph theory [3]. The selected Hamming/Fano construction in Example 8.7 supplies an example after an external code choice; it does not resolve intrinsic selection.

13.2 Observable and dynamic capacity

For a finite observation map $O : X \to Y$, one may define, when appropriate,

$$\mathrm{Cap}(O) := \log_2 |\operatorname{Im}(O)|.$$

For equal-size fibres, a corresponding lost-bit count is $\log_2 |X| - \mathrm{Cap}(O)$. These are proposed definitions, not consequences of the existing PRISM axioms.

For a finite self-map $\beta : X \to X$, a dynamic profile

$$C_\beta(t) := \log_2 |\operatorname{Im}(\beta^t)|$$

would summarize time-indexed image sizes. In the $n = 3$ coupled model, the cardinality sequence $|W_6| = 64$, $|\operatorname{range}(T_s)| = 16$, and $|\operatorname{range}(T_s^2)| = 4$ is directly verified in `PRISM.FourStateReduction` (`coupledUpdate_range_card`, `coupledUpdate_two_range_card`), so the base-two logarithms of the successive image sizes are 6, 4, and 2 for $t = 0, 1, 2$. More generally, by Equation (19) and Theorem 8.8, the universal odd-n coupled update has successive base-two logarithm image sizes $2n$, $n + 1$, and 2 across two updates.

13.3 Directed, weighted, and asynchronous network couplings

Having established in Theorem 9.2 the complete step-t image-size formula $|\mathrm{Im}(T_{G,s}^t)| = 2^{\mathrm{rank}_{\mathbb{F}_2}(A^t)+(n-1)\,\mathrm{rank}_{\mathbb{F}_2}((I+A)^t)}$ and the $(I+A)^k = 0 \pmod 2$ nilpotency criterion for synchronous updates on simple undirected graphs $G = (V, E)$, natural extensions include: (i) formalizing the matrix recurrence and rank-image laws for arbitrary $A \in \mathbb{F}_2^{m\times m}$ in Lean 4 using `Mathlib.LinearAlgebra.Matrix`; (ii) characterizing graph families whose binary adjacency matrices satisfy $(I+A)^k = 0$ with prescribed nilpotency index $k \le m$ [6, 3]; and (iii) analyzing asynchronous or block-sequential update schedules, where node-wise parity projection and neighbor summation no longer commute in a single global matrix step [10].

13.4 Discriminating controls

Any proposed geometric or informational significance should be tested against nearby comparison models: generic projectors of the same rank, quotients by other one-dimensional subspaces, even n, odd $n > 3$, alternative kernel vectors, and generic finite factor maps. Indeed, for any linear projector $E^2 = E$ on a binary vector space $V = \mathrm{Im}(E) \oplus \ker(E)$, the unshifted symmetric coupling acts as the direct product of the square-zero map $(u, v) \mapsto (u + v, u + v)$ on $(\mathrm{Im}\, E)^2$ and the coordinate swap on $(\ker E)^2$, while a common shift s sets both $\mathrm{Im}(E)$-coordinates to $E(s)$ after two steps and retains a persistent factor of $|\ker E|^2$ states. What the parity choice M_n adds to this general rank-$(n-1)$ projector mechanism is the specific identification of the one-dimensional kernel $\ker(M_n) = \langle \mathbf{1}_n \rangle$ with the antipodal direction of the prescribed hypercube Q_n. A feature is PRISM-specific only if the PRISM definitions select it rather than merely permit it. A more distant algebraic contrast is provided by cyclic projectors on max cones [11, Sections 1 and 4]; their idempotent semiring addition differs from characteristic-two cancellation.

14 Related Work

The mathematical core of PRISM lies at the intersection of several established subjects: finite dynamical systems over finite fields [1, 7]; linear and affine maps over $\mathbb{F}_2$ [12]; idempotent operators and kernel/image decompositions; binary even-weight and repetition codes [5]; factor maps and semiconjugacy [2, Definition 7.3.3]; affine conjugacy of finite dynamical systems; and formalized mathematics in Lean and Mathlib [8, 9].

PRISM does not claim that its constituent ingredients (binary vector spaces, parity checks, affine updates, finite quotients, or conjugacies) are individually new. Its structural contribution lies in their explicit combination within one finite dynamical construction. In particular, the local parity projector, the symmetric coupling T_s, the exact factor relation

$$\pi \circ T_s = g_{p(s)} \circ \pi,$$

the two-step collapse

$$T_s^2 = \iota_s \circ \pi,$$

and the shift conjugacies R_{s+t} together produce a closed hierarchy from microscopic state evolution to a four-state factor dynamics. The reduction is therefore not introduced as an external coarse-graining prescription: it is derived algebraically from the update rule itself. More generally, for any idempotent linear operator E on a binary vector space

$V = \mathrm{Im}(E) \oplus \ker(E)$, the unshifted symmetric coupling decomposes into the square-zero map $(u, v) \mapsto (u + v, u + v)$ on $(\mathrm{Im}\, E)^2$ and the involutive swap on $(\ker E)^2$, in accordance with the nilpotent-bijective decomposition of linear finite dynamical systems [7]; under a common shift s, T^2 sets both $\mathrm{Im}(E)$-coordinates to $E(s)$ and retains $|\ker E|^2$ persistent states (4 states whenever $\dim \ker E = 1$). The additional contribution of the parity projector M_n is to identify this one-dimensional kernel with the antipodal direction $\langle \mathbf{1}_n \rangle$ of the prescribed hypercube Q_n.

For the projector M_n (n odd), the nearest standard descriptions are linear algebra in characteristic two [12], binary coding theory [5], and antipodal quotients of binary hypercubes (folded cubes). For odd $n \geq 3$, the image of M_n is the binary even-weight code with parameters $[n, n-1, 2]_2$, whereas for $n = 1$ its image is the zero code $\{0\}$; for every odd $n \geq 1$, its kernel is the $[n, 1, n]_2$ binary repetition code. As shown in Section 8, the direct-sum decomposition $V_n = \ker(p_n) \oplus \langle \mathbf{1}_n \rangle$ bridges these static coding/hypercube quotients with the coupled dynamical reduction: one update of $T_{n,s}$ sets both nodes' even-parity coordinates to $M_n(a) + M_n(b) + M_n(s)$, and the second update fixes both even-parity coordinates to $M_n(s)$ independently of the initial state while recovering the initial parity pair in B.

The construction in Section 6 is a finite realization of factor dynamics and semiconjugacy [2, Definition 7.3.3]. With the discrete topology on the finite state spaces, the continuity condition in that definition is automatic. The map π is a surjective factor map, the reduced map $g_{p(s)}$ gives the induced dynamics on the parity factor, and ι_s is an injective canonical lift satisfying

$$\pi \circ \iota_s = \mathrm{id}\,.$$

The stronger identity $T_{n,s}^2 = \iota_{n,s} \circ \pi_n$ shows that every microscopic state lies in the anchor image $A_s = \mathrm{Im}(\iota_{n,s})$ by step two. In split coordinates $a = u + c\mathbf{1}_n$, $b = v + d\mathbf{1}_n$, and $s = w + e\mathbf{1}_n$, its first entry time into A_s is zero if $u = v = w$, one if $u = v \neq w$, and two if $u \neq v$; this uniform bound of two steps is sharp for odd $n \geq 3$, whereas for $n = 1$ every state is already an anchor. Thus PRISM distinguishes the transient relative displacement on the even-parity summand from the complete dynamics retained on the four-state factor.

A separate comparison concerns the conditions under which equivariant projections preserve the symmetry of an attractor [13, Theorem 2.6]. This concerns symmetry in real representation spaces, rather than the exact finite factorization established here.

The shift classification in Section 7 uses conjugacy as a bijective change of states [2, Definition 7.3.3]. Linear finite dynamical systems provide background on cycle structure and the decomposition into nilpotent and bijective components [7]; the affine shift conjugacies stated here are proved within PRISM. Its role here is to show that the eight apparent shift choices do not define eight distinct unlabeled dynamical systems: they are related by explicit self-inverse affine relabelings. This separates invariant dynamical structure from parameter-dependent presentation.

The Lean development described in Section 12 checks the project declarations listed in Tables 5–6, covering the parity projector, quotient reduction, $n = 3$ range cardinalities, shift conjugacies, general-coordinate dichotomy, and universal odd-n antipodal, affine-retraction, and entry-time theorems. Lean and Mathlib [8, 9] provide the verification methodology; they do not establish physical relevance or novelty by themselves. The contribution of the formalization is instead that the mathematical synthesis is represented as an auditable

collection of definitions and machine-checked theorems rather than as an analogy assembled only at the level of exposition.

Theoretical interfaces with coupled lattices and cellular automata [10, 6] and with stabilizer quantum channels and noiseless subsystems [14, 15, 16, 17] remain deliberately bounded. Such comparisons may identify shared algebraic structures, but no physical equivalence follows without an explicit correspondence preserving the relevant source-domain operations and observables.

15 Interfaces and Limitations

The finite model can support carefully delimited interfaces to other domains, but a valid bridge must specify a source-domain object, a PRISM object, an explicit correspondence, what structure the correspondence preserves, and what it does not establish.

At the algebraic level, p can be compared with a binary parity-check or syndrome map [15, Section 1.3], and $C(x) = x + \mathbf{1}$ with a global bit flip on binary labels. Stabilizer codes provide a further comparison at the level of binary representations [15, Section 3.4]; standard quantum error-correction background is given in [17, Sections 10.4–10.5]. These comparisons do not by themselves make the classical finite model PRISM a quantum code, make T_s a quantum channel without an explicit Hilbert-space embedding, or turn the period-two orbit into a physical time crystal.

15.1 Stabilizer measure-and-feedforward quantum channel bridge

To provide a concrete, mathematically well-defined interface to quantum information theory [14, 15, 16, 17] fulfilling all five bridge requirements above, we construct and analyze two distinct completely positive trace-preserving (CPTP) stabilizer Kraus channels (verified computationally in `notebooks/experiments/PRISM/quantum-channel-bridge/`): a single-node parity-measurement channel $\mathcal{E}_{M_n}$ on $(\mathbb{C}^2)^{\otimes n}$ and a coupled two-node coherent syndrome-reset channel $\mathcal{E}^{\text{coherent}}_{T_{n,s}}$ on $(\mathbb{C}^2)^{\otimes 2n}$. Keeping these two channels explicitly separate is essential because they measure and discard complementary registers. Formally, both channels are explicit PRISM specializations of the discrete-function-to-channel construction of Quillen and Skerrett [18, Definition 1 and Eq. (23)], which lifts any finite map $f : X \to X$ equipped with a partition $\{S_j\}$ of X into injective blocks to CPTP Kraus operators $L_j := \sum_{x \in S_j} |f(x)\rangle\langle x|$.

15.1.1 Channel 1: Single-node parity-measurement and conditional bit-flip channel $\mathcal{E}_{M_n}$

On the n-qubit Hilbert space $\mathcal{H}_n = (\mathbb{C}^2)^{\otimes n}$ with computational basis $\{|x\rangle : x \in V_n\}$, define the global Z-parity observable $S_Z := Z^{\otimes n}$ ($S_Z|x\rangle = (-1)^{p_n(x)}|x\rangle$), orthogonal parity projectors $P_{\text{even}} := \frac{1}{2}(I + Z^{\otimes n})$ and $P_{\text{odd}} := \frac{1}{2}(I - Z^{\otimes n})$, and global bit-flip unitary $X^{\otimes n}|x\rangle = |x + \mathbf{1}_n\rangle = |C_n(x)\rangle$. Define the single-node operator-sum map [14]

$$\mathcal{E}_{M_n}(\rho) := K_0 \rho K_0^\dagger + K_1 \rho K_1^\dagger, \qquad K_0 := P_{\text{even}}, \qquad K_1 := X^{\otimes n} P_{\text{odd}}. \tag{28}$$

Operationally, $\mathcal{E}_{M_n}$ performs a projective stabilizer measurement of $Z^{\otimes n}$, leaves the state untouched if the syndrome is $p_n = 0$, and applies the global bit flip $X^{\otimes n}$ if $p_n = 1$, then discards the 1-bit syndrome. In the partition prescription of [18], this corresponds to

choosing $f = M_n$ and partitioning V_n into the two injective parity blocks $\ker(p_n)$ (where $M_n = \mathrm{id}$) and $\mathbf{1}_n + \ker(p_n)$ (where M_n translates by $\mathbf{1}_n$); in the odd-n split basis $x = u + c\mathbf{1}_n$ ($u \in \ker(p_n)$), $\mathcal{E}_{M_n}$ acts as the identity on internal labels and resets the parity bit to 0.

Proposition 15.1 (Single-node stabilizer channel dichotomy)**.** For every $n \geq 1$, $\mathcal{E}_{M_n}$ is a valid CPTP channel satisfying $K_0^\dagger K_0 + K_1^\dagger K_1 = P_{\mathrm{even}} + P_{\mathrm{odd}} = I_{2^n}$ and reproducing the classical PRISM projector on diagonal states: $\mathcal{E}_{M_n}(|x\rangle\langle x|) = |M_n(x)\rangle\langle M_n(x)|$. Moreover:

(1) **Parity-Dephased vs. Intra-Sector Coherent:** Because the syndrome bit $r = p_n(x)$ is recorded by the environment, $\mathcal{E}_{M_n}(|x\rangle\langle x'|) = \delta_{p_n(x),\,p_n(x')}|M_n(x)\rangle\langle M_n(x')|$. Thus superpositions across even and odd parity sectors are dephased, whereas every pure quantum superposition $|\psi_{\mathrm{even}}\rangle = \sum_{u\in\ker(p_n)} \alpha_u|u\rangle$ inside the 2^{n-1}-dimensional even-parity subspace $\mathcal{H}_{\mathrm{even}} = \mathrm{Im}(P_{\mathrm{even}})$ (which for $n \geq 2$ has classical even-weight code parameters $[n, n-1, 2]_2$) is preserved noiselessly ($\mathcal{E}_{M_n}(\rho_{\mathrm{even}}) = \rho_{\mathrm{even}}$ for $\rho_{\mathrm{even}} = |\psi_{\mathrm{even}}\rangle\langle\psi_{\mathrm{even}}|$, fidelity $F = 1$).

(2) **Antipodal GHZ erasure:** For odd n, any antipodal superposition $|\mathrm{GHZ}_\phi(x)\rangle = \frac{1}{\sqrt{2}}(|x\rangle + e^{i\phi}|x + \mathbf{1}_n\rangle)$ has one component in $\mathcal{H}_{\mathrm{even}}$ and one in $\mathcal{H}_{\mathrm{odd}}$, so

$$\mathcal{E}_{M_n}(|\mathrm{GHZ}_\phi(x)\rangle\langle\mathrm{GHZ}_\phi(x)|) = |M_n(x)\rangle\langle M_n(x)|,$$

erasing the relative phase ϕ while outputting a pure state ($\mathrm{Tr}(\rho^2) = 1$).

(3) **Odd/even channel idempotence dichotomy:** Since $X^{\otimes n}Z^{\otimes n} = (-1)^n Z^{\otimes n}X^{\otimes n}$, we have $P_{\mathrm{even}}X^{\otimes n} = X^{\otimes n}P_{\mathrm{odd}}$ for odd n and $P_{\mathrm{even}}X^{\otimes n} = X^{\otimes n}P_{\mathrm{even}}$ for even n. Consequently,

$$\mathcal{E}_{M_n}^2 = \mathcal{E}_{M_n} \quad\Longleftrightarrow\quad K_0K_1 = K_1 \ \text{ and } \ K_1^2 = 0 \quad\Longleftrightarrow\quad n \text{ is odd.} \tag{29}$$

For even n, $K_0K_1 = 0$ and $K_1^2 = P_{\mathrm{odd}}$, so $\mathcal{E}_{M_n}$ is not a projection onto $\mathcal{H}_{\mathrm{even}}$.

15.1.2 Channel 2: Coupled two-node coherent syndrome-reset channel $\mathcal{E}^{\mathrm{coherent}}_{T_{n,s}}$

Whereas Channel 1 measures parity and preserves coherence inside $\mathcal{H}_{\mathrm{even}}$, the classical two-step factorization $T_{n,s}^2 = \iota_{n,s} \circ \pi_n$ for odd n erases the internal even-parity coordinates $(u, v) \in H^2$ ($H := \ker(p_n)$) and retains the 2-bit parity pair $(c, d) \in B$. If one applied a channel that measured (c, d), any superposition across distinct parity pairs would dephase. Instead, for odd $n \geq 3$, use the direct-sum isomorphism $V_n \cong H \oplus \mathbb{F}_2$ (Theorem 8.3) to factor the 2-node Hilbert space $\mathcal{H}_{2n} = (\mathbb{C}^2)^{\otimes 2n}$ into an internal register $\mathcal{H}_{\mathrm{int}} \cong \mathbb{C}^{2^{n-1}} \otimes \mathbb{C}^{2^{n-1}}$ with basis $|u, v\rangle$ ($u, v \in H$) and a 2-qubit logical parity register $\mathcal{H}_B \cong \mathbb{C}^2 \otimes \mathbb{C}^2$ with basis $|c, d\rangle$ ($c, d \in \mathbb{F}_2$). Matching [18, Definition 1 and Eq. (23)] applied to the classical split-coordinate map $f(u, v, c, d) = (u + v + w,\ u + v + w,\ g_e(c, d))$ partitioned by the second internal coordinate $S_v := \{(u, v, c, d) : u \in H,\ (c, d) \in B\}$ (on which f is injective for fixed v), define the coupled coherent channel $\mathcal{E}^{\mathrm{coherent}}_{T_{n,s}}$ on $\mathcal{H}_{2n}$ via 2^{n-1} Kraus operators $\{K_v\}_{v\in H}$:

$$K_v := \sum_{u\in H} |u + v + w,\ u + v + w\rangle\langle u, v|_{\mathrm{int}} \ \otimes\ U_{g_e}, \qquad U_{g_e}|c, d\rangle := |d + e,\ c + e\rangle, \tag{30}$$

where $w = M_n(s) \in H$ and $e = p_n(s) \in \mathbb{F}_2$. For each fixed $v \in H$, as u ranges over H, the output kets $|u + v + w, u + v + w\rangle_{\mathrm{int}}$ are mutually orthogonal. Consequently,

$K_v^\dagger K_v = \sum_{u\in H} |u,v\rangle\langle u,v|_{\text{int}} \otimes I_B$ is the orthogonal projector onto inputs with second internal coordinate v, and these projectors sum to the full identity $\sum_{v\in H} K_v^\dagger K_v = I_{2^{2n}}$ across all diagonal and off-diagonal entries, while the parity qubits (c,d) evolve unitarily via the involution U_{g_e} (SWAP followed by $X^{\otimes 2}$ if $e=1$).

In physical computational-basis coordinates $a,a',b,b' \in V_n$, identifying $v = M_n(b)$ makes the channel law completely explicit without reference to split coordinates:

$$\mathcal{E}_{T_{n,s}}^{\text{coherent}}(|a,b\rangle\langle a',b'|) = \delta_{M_n(b),\,M_n(b')}\,|T_{n,s}(a,b)\rangle\langle T_{n,s}(a',b')|. \tag{31}$$

Furthermore, the mechanism underlying two-step autonomous reset becomes transparent under the invertible affine basis permutation $W_w|u,v\rangle := |u+v,\, v+w\rangle$ on $H\times H$ with complete inverse $W_w^{-1}|P,Q\rangle = |P+Q+w,\, Q+w\rangle$. Setting $A_v := \sum_{u\in H}|u+v+w,u+v+w\rangle\langle u,v|$ and relabeling the Kraus index by $j = v+w \in H$ conjugates each internal Kraus operator to the **shift-and-reset normal form**:

$$L_j := W_w A_v W_w^\dagger = \sum_{P\in H} |0,P\rangle\langle P,j| \quad\Longrightarrow\quad \mathcal{S}(|P,Q\rangle\langle P',Q'|) = \delta_{Q,Q'}|0,P\rangle\langle 0,P'|, \tag{32}$$

which discards the second internal register Q, shifts P into the second position, and resets the first position to 0. Therefore $\mathcal{S}^2(\sigma) = |0,0\rangle\langle 0,0|\,\mathrm{Tr}(\sigma)$ after two steps (compare finite-time pure-state reset roots in [19] and dissipative subsystem cooling in [20]), while $U_{g_e}^2 = I_B$ on the logical register. Directly in the Kraus representation, if $t\in H$ labels the second application, then $K_tK_v = |w,w\rangle\langle t+v+w,\, v|_{\text{int}}\otimes I_B$, yielding for every input state ρ on $\mathcal{H}_{2n}\otimes\mathcal{H}_R$ (equivalently via $\mathrm{Ad}_{W_w^\dagger}\circ\mathcal{S}^2\circ\mathrm{Ad}_{W_w}$):

$$\begin{aligned} K_tK_v &= |w,w\rangle\langle t+v+w,\, v|_{\text{int}} \;\otimes\; I_B \\ \Longrightarrow\quad \Big((\mathcal{E}_{T_{n,s}}^{\text{coherent}})^2 \otimes \mathrm{id}_R\Big)(\rho) &= |w,w\rangle\langle w,w|_{\text{int}} \;\otimes\; \mathrm{Tr}_{\text{int}}(\rho). \end{aligned} \tag{33}$$

Equivalently, on physical matrix units,

$$\begin{aligned} (\mathcal{E}_{T_{n,s}}^{\text{coherent}})^2(|a,b\rangle\langle a',b'|) = \delta_{M_n(a),M_n(a')}\,\delta_{M_n(b),M_n(b')} \\ \times\, |\alpha_s(p_n(a)),\,\alpha_s(p_n(b))\rangle\langle \alpha_s(p_n(a')),\,\alpha_s(p_n(b'))|. \end{aligned}$$

Because the bras $\langle t+v+w,\, v|_{\text{int}}$ run bijectively through the entire orthonormal basis of $H\times H$ as (t,v) varies over $H\times H$, Equation (33) holds for every input density matrix ρ, including states entangled between $\mathcal{H}_{\text{int}}$, $\mathcal{H}_B$, and an external reference system R.

Thus $\mathcal{H}_B$ forms an exact 2-qubit noiseless subsystem [16] realizing a PRISM-specific partition instance of [18]: the four classical anchors $\{|\iota_{n,s}(q)\rangle\}_{q\in B} = \{|w,w\rangle_{\text{int}}\otimes|c,d\rangle_B\}$ span a 4-dimensional logical code space $A_s\subset\mathcal{H}_{2n}$ that is cooled back to $|w,w\rangle_{\text{int}}$ after two steps of $\mathcal{E}_{T_{n,s}}^{\text{coherent}}$ whenever noise acts strictly inside $\mathcal{H}_{\text{int}}$. Specifically, any pair of Pauli bit-flip errors $X^u\otimes X^v$ having even weight within each n-qubit node $(u,v\in H)$ shifts $(w,w)\mapsto(w+u,w+v)$ while leaving the parity qubits (c,d) invariant ($p_n(u) = p_n(v) = 0$). As shown in Figure 5, numerical verification at $n=3$ (6 qubits, 64×64 density matrices) across all 8 shifts $s\in V_3$ and all 16 node-wise even-weight bit-flip error pairs $(u,v)\in\ker(p_3)^2$ confirms that two applications of $\mathcal{E}_{T_{3,s}}^{\text{coherent}}$ restore the logical Bell states $|\Phi_L^+\rangle = \frac{1}{\sqrt{2}}(|\iota_{3,s}(0,0)\rangle + |\iota_{3,s}(1,1)\rangle)$ and $|\Psi_L^-\rangle = \frac{1}{\sqrt{2}}(|\iota_{3,s}(0,1)\rangle - |\iota_{3,s}(1,0)\rangle)$ to exact fidelity $F = 1.000000$ and purity $\mathrm{Tr}(\rho^2) = 1.000000$, compared with a mean initial fidelity of $F = 1/16 = 0.0625$ under a uniform choice of the 16 masks (where the identity mask has

initial fidelity 1 and each of the other 15 masks moves the encoded state to an orthogonal internal sector with fidelity 0). By contrast, odd-weight bit flips ($p_n(u) = 1$ or $p_n(v) = 1$) flip c or d and act as uncorrectable logical Pauli-X errors on $\mathcal{H}_B$; if physical qubits suffer independent bit-flip noise X with probability ϵ per qubit before ideal recovery, a logical flip occurs with probability

$$P_{\text{logical X}} = \Pr(\text{odd number of flips}) = \frac{1-(1-2\epsilon)^n}{2} = n\epsilon + O(\epsilon^2),$$

showing no distance suppression against isolated physical single-bit errors, and neither channel corrects phase-flip (Z) errors (compare autonomous bosonic memory encodings in [21]).

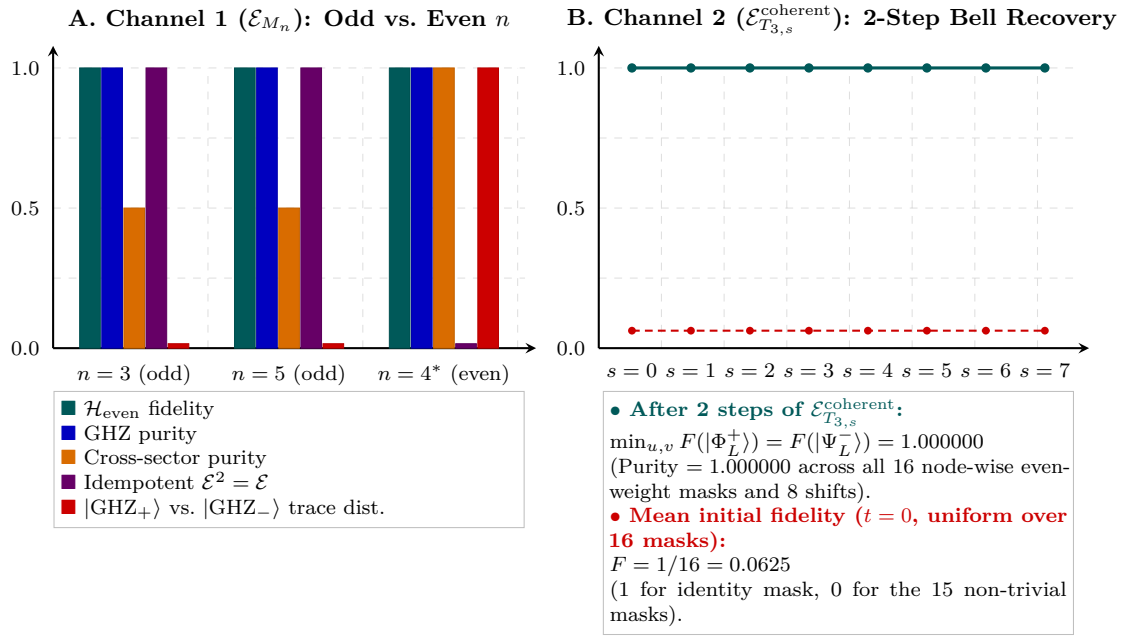


Figure 5: Quantum stabilizer channel bridge (`PRISM/quantum-channel-bridge`, Proposition 15.1 and Equation (33)). **(A)** Single-node channel $\mathcal{E}_{M_n}$ metrics across $n \in \{3, 5, 4^*\}$, showing exact $\mathcal{H}_{\text{even}}$ coherence preservation, antipodal GHZ phase erasure, and channel idempotence $\mathcal{E}^2_{M_n} = \mathcal{E}_{M_n}$ if and only if n is odd. **(B)** Coupled two-node coherent channel $\mathcal{E}^{\text{coherent}}_{T_{3,s}}$ 2-step autonomous recovery of logical Bell states $|\Phi^+_L\rangle$ and $|\Psi^-_L\rangle$ ($F = 1.000000$) across all 8 shifts $s \in V_3$ and all 16 pairs of bit-flip masks having even weight within each 3-qubit node.

15.1.3 Digital circuit compilation, parity-gate decoder, and resource comparison

Both channels admit ancilla-free compilations into standard digital gates (CNOT, X, computational-basis Z-measurement, classical outcome-controlled X, and single-wire reset to $|0\rangle$, expanding SWAP as 3 CNOTs) without analog phase calibration. Choose a pivot wire $c \in \{0, \ldots, n-1\}$ (for $n = 3$ with middle wire $c = 1$, the fan-in gate $G_3 = C(0 \to 1)C(2 \to 1)$ is the ideal nearest-neighbor parity gate of Kumar and Daraeizadeh [22, Section II, Eq. (1)]) and define the fan-in/fan-out CNOT decoder with $m := n - 1$:

$$G_n := \prod_{i \neq c} C(i \to c), \qquad F_n := \prod_{i \neq c} C(c \to i), \qquad D_n := F_n G_n.$$

Proposition 15.2 (Coordinate-decoder dichotomy and pruned reset-and-copy circuits)**.** For every $n \geq 1$, D_n is unitary with inverse $D_n^\dagger = G_n F_n$, mapping $|x\rangle \mapsto |y\rangle$ with $y_c = p_n(x)$ and $y_i = x_i + p_n(x)$ for $i \neq c$. Moreover, for odd $n \geq 3$:

(1) **Channel 1 decoding dichotomy and pruning:** Decoding with D_n, resetting the pivot wire c via $R_j := |0\rangle\langle j|_c \otimes I_{\text{non-}c}$, and applying $D_n^\dagger = G_n F_n$ implements $x \mapsto x + p_n(x)\mathbf{1}_n = M_n(x)$ ($\mathcal{E}_{M_n}$) if and only if n is odd; for even n, pivot reset instead implements $x \mapsto x + p_n(x)(\mathbf{1}_n + e_c) \neq M_n(x)$. Because wire c is $|0\rangle$ immediately after reset, the first inverse stage F_n acts as the identity and cancels identically, pruning Channel 1 to $G_n \to F_n \to \text{Reset}_c \to G_n$ ($3m$ CNOTs and 1 reset; 6 CNOTs at $n = 3$), while an ancilla-assisted parity measurement achieves n CNOTs with 1 extra clean qubit.

(2) **Channel 2 pruned reset-and-copy circuit:** Inside the decoded frame $D_n \otimes D_n$ separating internal non-pivot wires $(u, v) \in H^2$ from logical pivot wires $(c, d) \in B$, the shift-and-reset normal form Equation (32) ($\text{Ad}_{W_w^\dagger} \circ \mathcal{S} \circ \text{Ad}_{W_w}$) simplifies by eliminating the internal SWAP ($3m$ CNOTs) after resetting register B to $|0\rangle^{\otimes m}$ into the four-stage **reset-and-copy** circuit:

$$\text{CNOT}_{B\to A} \longrightarrow \text{Reset}_B \longrightarrow X_A^{w_{\text{np}}} \longrightarrow \text{CNOT}_{A\to B},$$

paired with U_{g_e} (SWAP_{c_A,c_B} plus $X_{c_A}X_{c_B}$ if $e = 1$) on the two pivot wires, where w_{np} denotes the m non-pivot coordinates of $w = M_n(s)$ (Hamming weight h). This implements $\mathcal{E}_{T_{n,s}}^{\text{coherent}}$ identically on all matrix units using $2m + 3$ decoded CNOTs ($10m+3$ physical CNOTs including the $8m$ entry/exit decoder boundaries; 23 physical CNOTs versus 29 unpruned at $n = 3$).

(3) **Pruned two-step endpoint baseline:** Implementing $\left(\mathcal{E}_{T_{n,s}}^{\text{coherent}}\right)^2$ directly without preserving the one-step action prunes on each node to $G_n \to F_n \to \text{Reset}_{\text{non-}c} \to F_n \to X^w$ using $6m$ physical CNOTs (12 at $n = 3$, compared with $8m = 16$ unpruned); omitting the first F_n ($4m$ CNOTs) fails by resetting x_i instead of u_i and destroying antipodal logical coherences.

Proof. Because gates within G_n commute and share only target c, and gates within F_n commute and share only control c, $G_n^2 = F_n^2 = I$, so $D_n^{-1} = D_n^\dagger = G_n F_n$ for every $n \geq 1$. After $R_j D_n |x\rangle = \delta_{j,p_n(x)}|y'\rangle$ with $y'_c = 0$ and $y'_i = x_i + p_n(x)$ ($i \neq c$), F_n acts trivially because its control wire is 0, and G_n writes $\sum_{i\neq c}(x_i + p_n(x)) = x_c + n\, p_n(x) \pmod 2$ onto wire c, which equals $(M_n(x))_c$ iff n is odd and leaves x_c unchanged when n is even, proving (1). On odd-n antipodal pairs $\frac{1}{\sqrt{2}}(|x\rangle + e^{i\phi}|x + \mathbf{1}_n\rangle)$, D_n maps the pivot wire to $\frac{1}{\sqrt{2}}(|p_n(x)\rangle + e^{i\phi}|p_n(x) + 1\rangle)_c$ unentangled from the constant non-pivot wires, so Reset_c erases ϕ in both sectors. For (2), following $\text{CNOT}_{B\to A}|u, v\rangle = |u + v, v\rangle$, Reset_B projects onto classical branch v and outputs $|u + v, 0\rangle$, whereupon $X_A^{w_{\text{np}}}$ and $\text{CNOT}_{A\to B}$ produce $|u + v + w, u + v + w\rangle$, matching A_v across all matrix units while eliminating the post-reset SWAP and second w-shift. For (3), per-node G_n sets wire c to $p_n(x)$, F_n converts non-pivot wires to $u_i = x_i + p_n(x)$, resetting non-pivot wires zeroes u, the second F_n copies $p_n(x)$ to every wire, and X^w produces $|w + p_n(x)\mathbf{1}_n\rangle = |\alpha_s(p_n(x))\rangle$ without altering $p_n(x)$-sector superpositions. □

The decoder constructions in Table 7 assume all-to-all CNOT connectivity (verified exhaustively in `docs/audit/compare_prism_digital_circuits.py` across all 4^n matrix

units for Channel 1 at $n \in \{3, 5\}$, all $8 \times 4^6 = 32{,}768$ shift-indexed 6-qubit matrix units for Channel 2 and its decoder-free specification Equation (31) at $n = 3$, and D_n unitarity/reset dichotomy for $n = 1, \ldots, 7$). Replacing resets by computational-basis Z-measurements and conditional X feedback on internal wires implements the same coherent channel (preserving all logical parity coherences and intra-fibre coherences retained by Equation (31)), whereas reading the two logical pivot wires preserves all 512 classical diagonals while destroying 6,144 off-diagonal matrix units across the eight shifts.

Proposition 15.3 (Local stabilizer-chain realization of the two-step endpoint)**.** For odd $n \geq 1$ and known even $w = M_n(s)$, define adjacent checks

$$S_i^{(w)} = (-1)^{w_i + w_{i+1}} Z_i Z_{i+1}, \qquad 0 \leq i < n - 1.$$

Their joint $+1$ code space is $\mathrm{span}\{|w\rangle, |w + \mathbf{1}_n\rangle\}$. Let $D(x)_i = x_i + x_{i+1}$, and for syndrome $r \in \mathbb{F}_2^{n-1}$ define

$$b_0 = 0, \qquad b_i = \sum_{j=0}^{i-1} r_j, \qquad u(r) = b + p_n(b)\mathbf{1}_n.$$

Measuring the checks, with outcome $r = D(x + w)$ on $|x\rangle$, and applying $X^{u(r)}$ implements the coherent single-node endpoint $|x\rangle \mapsto |w + p_n(x)\mathbf{1}_n\rangle$, retaining a matrix unit precisely when its two inputs have equal M_n image. Applying this channel independently to both nodes implements the two-step Channel 2 endpoint in Equation (33).

Proof. The adjacent-difference map D has rank $n - 1$ and kernel $\langle \mathbf{1}_n \rangle$, so the checks select exactly the stated two basis vectors. Since n is odd, $u(r)$ is the unique even vector with $D(u(r)) = r$. Writing $P_r^{(w)}$ for the joint syndrome projector, the operators $K_r = X^{u(r)} P_r^{(w)}$ obey $\sum_r K_r^\dagger K_r = I$. For input x, $u(D(x + w)) = M_n(x) + w$, giving the claimed output. A matrix unit $|x\rangle\langle y|$ survives the syndrome measurement iff $D(x) = D(y)$, equivalently $M_n(x) = M_n(y)$; within each such fibre the same correction preserves coherence. Tensoring the single-node channels gives Equation (33). □

Each node can use the interleaved line $d_0, a_0, d_1, a_1, \ldots, a_{n-2}, d_{n-1}$ with clean syndrome ancillas a_i. CNOTs $d_i \to a_i$ followed by $d_{i+1} \to a_i$ extract all adjacent parities in two disjoint CNOT layers. For both nodes this requires $4(n - 1)$ nearest-neighbor CNOTs, $2(n - 1)$ extra clean qubits, and $4n - 2$ physical qubits in total. Ancilla measurement, classical prefix decoding, conditional X correction, and ancilla cleanup complete the channel. The two-layer count excludes measurement, classical communication/decoding, and correction latency. One may measure raw $D(x)$, correct by $u(D(x))$, and apply the known X^w separately, as in the compiled construction. In Table 7, expanding each XOR-controlled correction into single-outcome-controlled X instructions gives $n^2 - 1$ data correction sites for the pair, plus $2m$ for ancilla cleanup; precomputing correction bits changes this instruction count without changing the channel.

These adjacent checks generate the same shifted repetition stabilizer group as the pivot-star checks [15]. On this code space, every node-wise even-weight X error is corrected; an odd-weight X error induces the logical complement $X^{\otimes n}$. A single Z_i commutes with every check and acts as a logical phase error, so the code has distance 1 against unrestricted Pauli errors. This realization supplies neither a new quantum code nor a fault-tolerance threshold. The pruned endpoint uses $6(n - 1)$ CNOTs with no extra qubits, data resets, and unrestricted pivot connectivity. The local chain exchanges clean ancillas

and measurement/feedback for fewer CNOTs and local connectivity; the differing budgets preclude an unqualified optimality ranking.

The exact checks in `notebooks/experiments/PRISM/tier-c-extensions/` match all 32,768 two-block matrix-unit/shift cases at $n = 3$ against both the two-step Kraus specification and the existing pruned endpoint circuit. Negative controls give 8,064 mismatches against the one-step channel and 1,024 discrepancies after additionally measuring one block's logical parity. Single-node fibre checks cover $n = 1, 3, 5, 7$, and basis decoding covers odd $n \leq 11$. At even $n = 4$, 0000 and 1111 have identical adjacent syndrome and parity, so the odd-n decoder cannot be extended by the same rule. These are ideal finite-channel checks, not tests of noisy hardware.

Circuit ($m := n-1$, odd $n \geq 3$)	Dec. CNOT	Phys. CNOT	Uncond. X	Meas.	Cond. X	Reset	Anc.
Single-node Channel 1 ($\mathcal{E}_{M_n}$; $n = 3 \Rightarrow m = 2$)							
Unpruned decoder / pivot reset ($D_n, \mathrm{Reset}_c, D_n^\dagger$)	—	$4m$ (8)	0	0	0	1	0
Pruned decoder / pivot reset ($G_n, F_n, \mathrm{Reset}_c, G_n$)	—	$3m$ (6)	0	0	0	1	0
In-place pivot measurement (G_n, meas. c, cond. $X^{\otimes n}, G_n$)	—	$2m$ (4)	0	1	n	0	0
Clean-ancilla parity measurement	—	n (3)	0	1	$n+1$	0	1
Coupled two-node Channel 2 ($\mathcal{E}^{\mathrm{coherent}}_{T_{n,s}}$; $h := \mathrm{wt}(w_{\mathrm{np}})$, $e := p_n(s)$, $+3$ = logical SWAP)							
Unpruned normal form ($\mathrm{Ad}_{W_w^\dagger} \circ \mathcal{S} \circ \mathrm{Ad}_{W_w}$)	$5m+3$ (13)	$13m+3$ (29)	$2h+2e$	0	0	m	0
Pruned reset-and-copy	$2m+3$ (7)	$10m+3$ (23)	$h+2e$	0	0	m	0
Direct internal syndrome measurement	$2m+3$ (7)	$10m+3$ (23)	$h+2e$	m	m	0	0
One reusable syndrome ancilla (sequential)	$2m+3$ (7)	$10m+3$ (23)	$h+2e$	m	$3m$	0	1
Separate two-step endpoint baseline ($\left(\mathcal{E}^{\mathrm{coherent}}_{T_{n,s}}\right)^2$ directly; $8m = 16$ unpruned vs. $6m = 12$ pruned at $n = 3$)							
Pruned per-node $G_n, F_n, \mathrm{Reset}_{\text{non-}c}, F_n, X^w$	—	$6m$ (12)	$2\,\mathrm{wt}(w)$	0	0	$2m$	0
Interleaved nearest-neighbor stabilizer chain	—	$4m$ (8)	$2\,\mathrm{wt}(w)$	$2m$	$n^2 - 1 + 2m$	0	$2m$

Table 7: Instruction-site resource comparison for ideal digital realizations of PRISM Channels 1 and 2 ($n = 3$ CNOT counts shown in parentheses). Decoder rows assume all-to-all CNOT connectivity; the last row uses an interleaved nearest-neighbor data/ancilla line. Counts describe compiled constructions, with different ancilla and feedback budgets, rather than hardware lower bounds or noise thresholds.

15.2 Factor-dynamics interface and model limitations

The factor map π partitions the finite state space into parity-pair fibres. The relation $\pi \circ T_s = g_{p(s)} \circ \pi$ specifies exactly how these fibres evolve, and $T_s^2 = \iota_s \circ \pi$ identifies the canonical representatives reached after two updates. These finite algebraic identities supply the interface to factor dynamics; additional geometric or physical structures require explicit definitions and correspondence results such as Propositions 15.1 and 15.2 and Equation (33).

The principal limitations are explicit. The core PRISM dynamics is finite and deterministic. The update rules are model choices rather than derived necessities. Iteration order supplies a discrete event ordering but not a derivation of physical time. The current theory contains no continuum limit, no empirical map, and no derived physical spacetime correspondence. Formal verification applies to the stated mathematical theorems under their actual definitions and dependencies; it does not validate an ontology.

16 Conclusion

PRISM's strongest content is a compact finite-dynamics theorem package over $\mathbb{F}_2$ together with its graph-coupled generalization, matched-workload complexity characterization, $[9, 4, 4]_2$ operator-space product code, and digital stabilizer quantum-channel bridge. The three-coordinate parity operator M is an exact idempotent projector onto $\ker(p)$ with

complementary fibres. Its affine extension is eventually involutive. Symmetric coupling introduces a conserved total parity and an exact two-step collapse to canonical anchors. The resulting dynamics closes on a four-state quotient, and every shift choice is conjugate to every other by an explicit bijective relabeling. The same projector mechanism exhibits a sharp even/odd coordinate-count dichotomy: for every odd n, M_n realizes the canonical even-parity section of the antipodal hypercube quotient $V_n/\langle \mathbf{1}_n \rangle \cong \ker(p_n)$, and after two coupled updates $T^2_{n,s}$ both even-parity coordinates equal $M_n(s)$ independently of their initial values while the original parity pair in B is recovered; for every positive even n, by contrast, $T^2_{n,s}(a,b) = (M_n(s), M_n(s))$ collapses all 2^{2n} states to a single constant state. Extending the coupling to an arbitrary m-node simple undirected graph $G = (V, E)$ yields the exact step-t image formula $|\mathrm{Im}(T^t_{G,s})| = 2^{\mathrm{rank}_{\mathbb{F}_2}(A^t)+(n-1)\,\mathrm{rank}_{\mathbb{F}_2}((I+A)^t)}$ for every odd $n \geq 1$ and proves that for odd $n \geq 3$, uniform recovery from the initial m-bit parity vector holds if and only if $I + A$ is nilpotent over $\mathbb{F}_2$. Finally, the controlled benchmarks, two-dimensional product-code and plaquette duality, and CPTP stabilizer Kraus channels and pruned CNOT circuits quantify the computational, coding-theoretic, and quantum-information behavior of the reduction.

The significance of these results is mathematical before it is interpretive. The direct-sum splitting $V_n = \ker(p_n) \oplus \langle \mathbf{1}_n \rangle$, universal odd-$n$ affine retraction, universal even-n constant collapse, multi-node $\mathbb{F}_2$ rank-image law, and shift conjugacy say precisely how much of the microscopic dynamics is transient relative even-parity displacement, how much is persistent parity-factor structure, and how much is shift-dependent state labeling. The reported Lean formalization and reproducible computational suite make the proof and verification status of every claim auditable.

References

[1] B. Elspas. The theory of autonomous linear sequential networks. *IRE Transactions on Circuit Theory*, 6(1):45–60, 1959.

[2] Boris Hasselblatt and Anatole Katok. *A First Course in Dynamics: With a Panorama of Recent Developments*. Cambridge University Press, Cambridge, 2003.

[3] C. Godsil and G. Royle. *Algebraic Graph Theory*, volume 207 of *Graduate Texts in Mathematics*. Springer, New York, 2001.

[4] Andries E. Brouwer. Clebsch graph. Researcher's graph description, Eindhoven University of Technology. Accessed November 16, 2026; distinguishes the folded five-cube from its complement.

[5] F. J. MacWilliams and N. J. A. Sloane. *The Theory of Error-Correcting Codes*. North-Holland, Amsterdam, 1977.

[6] O. Martin, A. M. Odlyzko, and S. Wolfram. Algebraic properties of cellular automata. *Communications in Mathematical Physics*, 93(2):219–258, 1984.

[7] R. A. Hernández-Toledo. Linear finite dynamical systems. *Communications in Algebra*, 33(9):2977–2989, 2005.

[8] L. de Moura and S. Ullrich. The Lean 4 theorem prover and programming language. In *Automated Deduction – CADE 28*, volume 12699 of *LNCS*, pages 625–635. Springer, 2021.

[9] The mathlib Community. The Lean mathematical library. In *Certified Programs and Proofs (CPP 2020)*, pages 367–381. ACM, 2020.

[10] J. Jost and M. P. Joy. Spectral properties and synchronization in coupled map lattices. *Physical Review E*, 65(1):016201, 2002.

[11] Sergei Sergeev. Multiorder, Kleene stars and cyclic projectors in the geometry of max cones. In *Tropical and Idempotent Mathematics*, volume 495 of *Contemporary Mathematics*, pages 317–342. American Mathematical Society, 2009.

[12] R. Lidl and H. Niederreiter. *Finite Fields*. Cambridge University Press, 2nd edition, 1997.

[13] Jeffrey H. Schenker and James W. Swift. Observing the symmetry of attractors. *Physica D: Nonlinear Phenomena*, 114(3–4):315–337, 1998.

[14] K. Kraus. *States, Effects, and Operations: Fundamental Notions of Quantum Theory*, volume 190 of *Lecture Notes in Physics*. Springer, Berlin, 1983.

[15] D. Gottesman. *Stabilizer Codes and Quantum Error Correction*. PhD thesis, California Institute of Technology, 1997. arXiv:quant-ph/9705052.

[16] E. Knill, R. Laflamme, and L. Viola. Theory of quantum error correction for general noise. *Physical Review Letters*, 84(11):2525–2528, 2000.

[17] M. A. Nielsen and I. L. Chuang. *Quantum Computation and Quantum Information*. Cambridge University Press, 10th anniversary edition, 2010.

[18] A. C. Quillen and Nathan Skerrett. Generating quantum channels from functions on discrete sets. *Quantum Information Processing*, 23:55, 2024. arXiv:2308.06084.

[19] B. V. Rajarama Bhat, Robin Hillier, Nirupama Mallick, and Vijaya Kumar U. Roots of completely positive maps. *Linear Algebra and its Applications*, 587:143–165, 2020. arXiv:1812.08123.

[20] Peter D. Johnson, Francesco Ticozzi, and Lorenza Viola. Exact stabilization of entangled states in finite time by dissipative quantum circuits. *Physical Review A*, 96:012308, 2017. arXiv:1703.06183.

[21] Zaki Leghtas, Gerhard Kirchmair, Brian Vlastakis, Robert Schoelkopf, Michel Devoret, and Mazyar Mirrahimi. Hardware-efficient autonomous quantum memory protection. *Physical Review Letters*, 111:120501, 2013. arXiv:1207.0679.

[22] P. Kumar and S. Daraeizadeh. Parity-based mirror inversion for efficient quantum state transfer and computation in nearest-neighbor arrays. *Physical Review A*, 91:042310, 2015.